

Stochastic modeling of paraxial x-ray superfluorescence

Andrei Benediktovitch,^{1,*} Stasis Chuchurka,¹ Špela Krušič,² Aliaksei Halavanau,³ and Nina Rohringer^{1,4}

¹*Deutsches Elektronen-Synchrotron DESY, Hamburg 22607, Germany*

²*Jožef Stefan Institute, Ljubljana 1000, Slovenia*

³*Accelerator Research Division, SLAC National Accelerator Laboratory, Menlo Park, CA 94025*

⁴*Department of Physics, Universität Hamburg, Hamburg 22761, Germany*

Abstract

An approach to modeling the dynamics of x-ray amplified spontaneous emission (ASE) and superfluorescence (SF) – collective x-ray fluorescence emission phenomenon initiated by intense X-ray Free Electron Laser pump pulse – is developed based on Stochastic Partial Differential Equations. The equations are derived from the first principles, the approximations, derivation steps, and extensions specific to stimulated x-ray emission are performed. The resulting equations have a form of three-dimensional – in paraxial approximation – Maxwell-Bloch equations augmented with the noise terms for both field and atomic variables. The derived noise terms possess specific correlation properties that enable correct reconstruction of spontaneous emission. As a result, the developed formalism is uniformly suitable for the description of all stages of the stimulated x-ray emission: spontaneous emission, ASE, and superfluorescence. Our numerical scheme circumvents the problem of run-away trajectories which are typical for stochastic differential equations based on positive P-representations. Numerical example illustrating multiple properties of the emitted field – e.g., spatio-temporal coherence – are presented. We expect that the developed formalism will form a solid base for interpreting stimulated x-ray emission spectroscopy data, modeling the X-ray Laser Oscillator (XLO), and describing other experiments that employ x-ray superfluorescence phenomena.

* andrei.benediktovitch@desy.de

I. INTRODUCTION

The X-ray radiation wavelength is naturally suited for studying matter at an atomic resolution and sub-fs time-scale. At the same time, the short radiation wavelength results in weak interaction with matter, thus most of the widespread x-ray analytical techniques [1] rely on linear x-ray – matter interaction processes. The situation is currently changing due to the construction of X-ray Free Electron Lasers (XFELs) [2–6] in the last decade. XFELs are opening the realm of exploration of high-intensity, nonlinear x-ray–matter interaction phenomena. The bright and fs-short XFEL pulses drive the matter into previously unexplored states and enable unique insights into its structure and dynamics [7–12].

For instance, a phenomenon that could not be studied before the operation of XFELs is the population inversion of the inner-shell atomic levels. It now can be achieved as a result of massive inner-shell photoionization along the path of a focused pump beam. In the optical domain, a medium that is kept in a population-inverted state and placed in a resonator forms a classical laser oscillator. In the x-ray domain, however, sustaining population inversion is not realistic due to fs-fast decay processes, and creating an x-ray resonator is challenging. Thus, we will consider the case when the population inversion is produced in a swept and transient manner, where the x-ray emission process starts from an isotropic spontaneous x-ray fluorescence. Upon propagating through the pencil-shaped core-hole excited medium, the spontaneous radiation is exponentially amplified until saturation, and yields short directed x-ray bursts. We note that this mechanism is similar to a single pass, high-gain XFEL. We later refer to the exponential amplification regime as ASE regime and the saturation as SF regime.

The soft x-ray SF was first realized in Ne gas [13], [14] – the observed radiation emission was also referred to as atomic x-ray lasing. Subsequent experiments have demonstrated hard x-ray SF for solid targets [15], [16] and liquid jets [17], [18]. Several applications for these types of x-ray pulses have been proposed so far. The directivity and the high intensity of the SF pulses facilitate high signal-to-noise ratio measurements, which is beneficial in x-ray spectroscopy. For instance, it was experimentally demonstrated in [17] that the chemical shift is preserved upon the fluorescence amplification. Subsequently, it was shown that weaker x-ray emission lines could be seeded and thus selected from other lines [18]. The development of these techniques – commonly referred to as stimulated X-ray Emission Spectroscopy (sXES)

– is one of the future directions of x-ray spectroscopy development at XFELs [10]. Similarly, the process of SF may be used as a source of x-ray radiation with unique characteristics. In [16], it was demonstrated that employing an XFEL pump pulse with two strong SASE spikes results in two-pulse x-ray SF, where the resulting spectrum showed an interference pattern with a very high fringe contrast. Further improvement of this technique may create the x-ray sources needed for coherent nonlinear spectroscopy techniques [19]. Finally, in Ref. [20] hard x-ray atomic lasing medium, operating in ASE or SF regimes, was placed in the Bragg cavity, thus forming an X-ray Laser Oscillator (XLO). After several cycles in the XLO, the emitted radiation is expected to become spatially and temporally coherent, similar or better than cavity-based XFEL pulses [21–24].

The interpretation of the sXES data, as well as modeling of x-ray SF-based sources like XLO, strongly benefits from predictive, quantitative modeling. In general, the phenomenon can be considered as a particular case of superradiance, which historically attracted a lot of interest, see e.g. Refs [25], [26], [27]. A full quantum description of the interaction between the modes of electromagnetic field continuum and an ensemble of few-level emitters could be performed for certain particular cases, assuming the permutational invariance of emitters [28], [29], [30] or restricting the evolution to early time [31], [32]. However, these methods could not be directly applied to our problems, since we are interested in systems containing $\sim 10^{12}$ emitters. Hence, we have to use a continuum-media method of description. This should encompass, in the general case, the dynamics of pumping and building up the transient population inversion, the initial stage of spontaneous emission, subsequent propagation and diffraction of the amplified emitted field, and the dynamics in the nonlinear saturation regime. Here we note once again the similarity to classical XFEL modelling. If quantum properties of the electromagnetic field could be neglected, the continuum-media description could be done with help of optical Maxwell-Bloch (MB) equations [33]. However, in the case of SF, no atomic coherences nor emitted fields are initially present, hence homogeneous MB equations would produce a trivial solution. Thus, combining the MB equations with quantum effects responsible for spontaneous emission that triggers SF is necessary.

A rigorous description of both quantum and classical effects, e.g. diffraction is possible in the ASE regime. In this case, the emitted fields are not strong enough to cause a change in the population inversion, and the equations for field and atomic operators become linear. Under these conditions, analytical expressions for emitted field properties could be derived

for various shapes of the inverted medium [34], [35], [36]. Once the emitted field becomes strong, the ASE regime transforms into a saturation, SF regime where nonlinear effects play an important role, and the quantum fluctuations have much smaller contributions compared to interaction with the emitted field. In the case of instantaneous excitation of atoms, the influence of quantum fluctuations was shown to be equivalent to the distribution of initial conditions for the MB equations. In two-level systems, the distribution of initial conditions could be mapped onto the distribution of the tipping Bloch-vector around the pole of the Bloch sphere [26]. Within this approach, for certain systems emitting in the optical domain, the effective tipping angle could be observed experimentally [37]. The numerical modeling of SF including diffraction effects is possible in paraxial approximation [26], [38] as well as within rigorous finite-difference time-domain methods [39], [40]. However, in the x-ray domain, the fs-rapid depopulation of the core-excited states – due to the Auger-Meitner and radiative decays caused by fluorescence emission in 4π solid angle – does not allow for the use of the instantaneous excitation approximation. In this case, pumping, decays, and SF processes take place on the same time scale. In addition, different regions of the medium may simultaneously experience evolution in different regimes – e.g., the central part may experience saturation, while the edges may be still within ASE. Hence a formalism that enables a uniformly-suitable description of both quantum spontaneous emission and semi-classical MB-like behavior is needed.

It is possible to modify semi-classical equations in a way to include quantum effects responsible for spontaneous emission, e.g: to augment the MB equations with noise terms in the field equations [41], or in the atomic equations [42]; to include stochastic relaxation terms in the atomic equations, and perform rescaling of the electric field – so-called Ehrenfest+R method [43], [44]; and other ways [45]. However, since those methods were not derived from the first principles but rather phenomenologically, they possess certain limitations. Among those methods, the approach based on augmenting the MB equations with phenomenological noise terms [42] became most widespread and was applied for a series of problems [46], [47], [48], [49], [17], [50], [16]. This approach has the same computational complexity as MB equations, and describes well the nonlinear dynamics in the saturation stage, however, has deficiencies in the description of the initial spontaneous-emission dominated stage. Namely, as discussed in [51], [52], the resulting temporal profile of the spontaneous emission is not reproduced correctly. A correct description of the spontaneous emission and cross-over

to MB equations can be realized based on solving equations for the correlation function of the field and atomic coherences [52], this approach was applied for the description of several systems [53], [54]. However, the resulting numerical scheme is more computationally expensive since two-point quantities should be computed. Moreover, extending this approach beyond two-level systems is challenging since the factorization of higher-order correlation functions into one-point and two-point correlation functions – which is crucial to obtain a closed system of equations – becomes problematic even for the three-level Λ systems.

In this paper, we aim to present an approach that would be general enough to describe spontaneous x-ray emission, ASE, and SF under realistic conditions and would also be free from uncontrollable approximations. We build on the general formalism presented in the series of papers [55], [56], [57], and apply it to the particular case of lasing in the copper medium. Namely, we consider a typical LCLS-like XFEL-pump pulse, and medium parameters, that result in pencil-shaped geometry. In this case, we can apply the paraxial approximation and – due to a short pump-pulse duration as well as rapid decay compared to the propagation time – neglect the back-propagating wave and thus take advantage of using retarded time. Under these simplifications, we obtain equations that look like MB with noise terms – however, the derived noise terms possess non-trivial correlation properties and can correctly reproduce the spontaneous emission. Due to the noise correlation properties, the numerical implementation of resulting equations should be done with care and is discussed in the paper. The paper is organized as follows: In Sec. II, the general formalism from [55], [56] is applied to our case to form a system of Stochastic Partial Differential Equations (SPDE). In Appendix B, the numerical scheme for solving the SPDE in retarded time is presented. In Sec. III, the obtained SPDE are further specified for the particular case of Cu- $K\alpha_1$ level scheme and relevant pump, decay, and decoherence processes; the details of which are discussed in Appendices C and D. Finally, in Sec. IV, an example of numerical modeling is presented, and the relation between SPDE output and physical observables of interest is discussed.

II. STOCHASTIC PARTIAL DIFFERENTIAL EQUATIONS FOR X-RAY – MULTILEVEL ATOMS INTERACTION IN PARAXIAL APPROXIMATION

The stochastic approach to modeling interaction between the quantized electromagnetic field and ensemble of atoms was described in [55], [56]. Here, we start from the general form of SPDE derived in [56] and perform a series of approximations relevant for the paraxial x-ray SF problem.

A. Stochastic differential equations for general case

Following [56], the description of field-atom quantum system is based on stochastic variables that enable us to get the values of quantum-mechanical observables. Namely, the electromagnetic field is described by the stochastic fields $\mathcal{D}(\mathbf{r}, t)$ and $\mathcal{B}(\mathbf{r}, t)$. From a set of realizations (trajectories) of these stochastic fields one can get the statistical properties of the electric displacement field and magnetic field, e.g.:

$$\langle \left(\widehat{\mathcal{D}}^{(-)}(\mathbf{r}_1, t_1) \right)^n \left(\widehat{\mathcal{D}}^{(+)}(\mathbf{r}_2, t_2) \right)^m \rangle_{QM} = \langle \left(\mathcal{D}^{(-)}(\mathbf{r}_1, t_1) \right)^n \left(\mathcal{D}^{(+)}(\mathbf{r}_2, t_2) \right)^m \rangle_{\text{trajectories}}. \quad (1)$$

Here (\pm) stands for positive- and negative-frequency components of the field, $\langle \rangle_{QM}$ denotes to quantum-mechanical expectation value of an observable, $\langle \rangle_{\text{trajectories}}$ denotes averaging over stochastic trajectories. The atomic ensemble is described by a stochastic matrix field $P_{pq}(\mathbf{r}, t)$, from which one can get observables at continuous-media level of description. Originally in [56], the stochastic matrix field was denoted by $\rho_{pq}(\mathbf{r}, t)$. In this article, we reserve $\rho_{pq}(\mathbf{r}, t)$ for the normalized stochastic matrix (13)-(16) that we introduce later. E.g., an expectation value of continuous-media average of a one-particle observable $\hat{\mathcal{O}}$ is expressed as

$$\mathcal{O}(\mathbf{r}, t) \equiv \langle \sum_a \text{Tr} \left(\hat{\mathcal{O}}_a(t) \hat{\rho} \right) \delta(\mathbf{r} - \mathbf{r}_a) \rangle_{\text{positions}} = \sum_{p,q} \mathcal{O}_{qp} \langle P_{pq}(\mathbf{r}, t) \rangle_{\text{trajectories}} \quad (2)$$

Here index a stands for atoms within the atomic ensemble, $\langle \rangle_{\text{positions}}$ denotes averaging over atomic positions \mathbf{r}_a that are assumed to be random (like in ideal gas), indexes p, q denote states corresponding to energy levels of isolated atom, \mathcal{O}_{qp} is a matrix element of the operator $\hat{\mathcal{O}}$, all atoms are assumed to be identical in terms of transition energies and dipole moments.

In [56] it was shown that SPDE for $\mathcal{D}(\mathbf{r}, t)$, $\mathcal{B}(\mathbf{r}, t)$, $P_{pq}(\mathbf{r}, t)$ has a form closely resembling the semi-classical Maxwell-Bloch system of equations augmented with noise terms. Namely, the SDE for stochastic fields can be represented in a form resembling Maxwell equations:

$$\nabla \cdot \mathcal{D}(\mathbf{r}, t) = 0, \quad (3)$$

$$\nabla \cdot \mathcal{B}(\mathbf{r}, t) = 0, \quad (4)$$

$$-\varepsilon_0 \frac{\partial \mathcal{B}(\mathbf{r}, t)}{\partial t} = \nabla \times (\varepsilon^{-1}(\mathbf{r}, t) \mathcal{D}(\mathbf{r}, t) - \delta \mathcal{P}(\mathbf{r}, t)), \quad (5)$$

$$\frac{\partial \mathcal{D}(\mathbf{r}, t)}{\partial t} = \nabla \times (\mu_0^{-1} \mathcal{B}(\mathbf{r}, t) - \delta \mathcal{M}(\mathbf{r}, t)), \quad (6)$$

with an additional stochastic contribution to polarization $\delta \mathcal{P}(\mathbf{r}, t)$ and magnetization $\delta \mathcal{M}(\mathbf{r}, t)$ terms:

$$\delta \mathcal{P}(\mathbf{r}, t) = \sum_{p,q} \mathbf{d}_{pq} P_{qp}(\mathbf{r}, t) + \frac{1}{2} (\mathbf{f}(\mathbf{r}, t) + \mathbf{f}^\dagger(\mathbf{r}, t)), \quad (7)$$

$$\delta \mathcal{M}(\mathbf{r}, t) = \frac{c}{i(2\pi)^2} \nabla \times \int \frac{\mathbf{f}(\mathbf{r}', t) - \mathbf{f}^\dagger(\mathbf{r}', t)}{|\mathbf{r} - \mathbf{r}'|^2} d\mathbf{r}'. \quad (8)$$

The SPDE for $\rho_{pq}(\mathbf{r}, t)$ has the form of a semi-classical Bloch equation with additional noise-terms:

$$\begin{aligned} \frac{\partial}{\partial t} P_{pq}(\mathbf{r}, t) &= -i (\omega_p - \omega_q) P_{pq}(\mathbf{r}, t) \\ &+ \frac{1}{2} \sum_{i,j} \left(2\Gamma_{iqjq}(\mathbf{r}, t) P_{ij}(\mathbf{r}, t) - \Gamma_{pjij}(\mathbf{r}, t) P_{iq}(\mathbf{r}, t) - P_{pi}(\mathbf{r}, t) \Gamma_{ijjq}(\mathbf{r}, t) \right) \\ &+ \frac{i}{\hbar \varepsilon_0} \mathcal{D}(\mathbf{r}, t) \sum_r (\mathbf{d}_{pr} P_{rq}(\mathbf{r}, t) - P_{pr}(\mathbf{r}, t) \mathbf{d}_{rq}) \\ &+ \sum_r (\mathbf{f}^*(\mathbf{r}, t) \mathbf{d}_{pr} P_{rq}(\mathbf{r}, t) + P_{pr}(\mathbf{r}, t) \mathbf{d}_{rq} \mathbf{f}^\dagger(\mathbf{r}, t)). \end{aligned} \quad (9)$$

The noise terms here and in field equations (3)-(8) are independent normalized complex vector Gaussian white noise terms with the following correlation properties:

$$\langle \mathbf{f}(\mathbf{r}, t) \otimes \mathbf{f}(\mathbf{r}', t') \rangle = \langle \mathbf{f}^\dagger(\mathbf{r}, t) \otimes \mathbf{f}^\dagger(\mathbf{r}', t') \rangle = \quad (10)$$

$$\langle \mathbf{f}(\mathbf{r}, t) \otimes \mathbf{f}^\dagger(\mathbf{r}', t') \rangle = \langle \mathbf{f}^*(\mathbf{r}, t) \otimes \mathbf{f}^\dagger(\mathbf{r}', t') \rangle = 0,$$

$$\langle \mathbf{f}(\mathbf{r}, t) \otimes \mathbf{f}^*(\mathbf{r}', t') \rangle = \langle \mathbf{f}^\dagger(\mathbf{r}, t) \otimes \mathbf{f}^*(\mathbf{r}', t') \rangle = \delta(\mathbf{r} - \mathbf{r}') \delta(t - t') \mathbb{I}.$$

Here, the delta functions of time differences tell us that the time integration involving these noise terms must be interpreted in one of two ways, namely, Ito or Stratonovich sense. The transition from one way to another typically introduces additional deterministic terms, which equal zero in our particular case. In contrast, the delta functions for coordinate distances have a different interpretation and must be seen as continuous bell functions of a small variance tending to zero.

In eqs. (3)-(10) the following quantities were used: \mathbf{d}_{pq} is the dipole matrix element for transition between atomic levels p, q ; $\hbar\omega_p$ stands for the energy of the level p ; ε is the permittivity of the medium conditioned by mechanisms other than transition between considered atomic levels; Γ_{ijkl} are rates responsible for incoherent processes such as pumping, decay, decoherence due to ionization and Auger decay (see [55] for detailed discussion); N is the total number of atoms in the ensemble.

B. Variables within slowly-varying envelope approximation

A system of SPDE (3)-(10) is applicable to the general case of interaction between electromagnetic field and ensemble of large amount of atoms at continuous-media level of description. For the specific case of paraxial x-ray superfluorescence, we can apply a series of simplifications. The pumping by a focused XFEL beam determines the pencil-shape geometry of the excited medium. According to [58], for gaussian beams with beam waist $w_0 > 100\lambda$ (λ is radiation wavelength), the difference between the solutions of full Maxwell equations and the paraxial scalar wave equations is less than few percent. Since the XFEL beam focus size – even for best x-ray focusing optics – is much larger than the wavelength [59], [60], we will use the paraxial approximation and represent field $\mathcal{D}(\mathbf{r}, t)$ as

$$\mathcal{D}(\mathbf{r}, t) = \sum_s (D_s^{(+)}(\mathbf{r}, t) e^{i(k_0 z - \omega_0 t)} \mathbf{e}_s + D_s^{(-)}(\mathbf{r}, t) e^{-i(k_0 z - \omega_0 t)} \mathbf{e}_s^*), \quad (11)$$

here s enumerates two orthogonal unit polarization vectors \mathbf{e}_s ; $k_0 = \omega_0/c$ is the wavevector of a carrier wave, its propagation direction is denoted as z , vectors \mathbf{e}_s are orthogonal to z ; $D_s^{(\pm)}(\mathbf{r}, t)$ are slowly-varying envelopes, superscript (\pm) stands for positive- and negative-frequency components of the field.

To simplify the general equation for the atomic variables (9), we assume that the atomic

levels can be grouped in two manifolds: excited (upper) levels $\mathbf{e} = \{e_1, e_2, \dots, e_{N_e}\}$ and ground (lower) levels $\mathbf{g} = \{g_1, g_2, \dots, g_{N_g}\}$. E.g., for the case of x-ray superfluorescence at K- α line, levels \mathbf{e} correspond to atomic states with hole in the K-shell, levels \mathbf{g} – to states with hole in L-shell, this example will be described in more details in Sec. III. In this way, the $(N_e + N_g) \times (N_e + N_g)$ matrix built of $P_{ij}(\mathbf{r}, t)$ can be separated into blocks:

$$P_{ij} = \begin{pmatrix} P_{gg'} & P_{ge} \\ P_{eg} & P_{ee'} \end{pmatrix}, \quad (12)$$

here elements $P_{ee'}$ ($P_{gg'}$) are related to excited (ground) state populations (diagonal elements) and coherences within the excited (ground) states (off-diagonal elements), while the elements P_{eg}, P_{ge} are responsible for coherence between the excited and ground levels. We assume that radiative transitions are essential only between the excited and ground levels, and that the energy difference between the these groups of levels is close to ω_0 . In this way, the components of P_{ij} can be expressed in terms of slowly-varying components as

$$P_{ee'}(\mathbf{r}, t) = n(\mathbf{r})\rho_{ee'}(\mathbf{r}, t), \quad (13)$$

$$P_{eg}(\mathbf{r}, t) = n(\mathbf{r})\rho_{eg}(\mathbf{r}, t)e^{i(k_0 z - \omega_0 t)}, \quad (14)$$

$$P_{ge}(\mathbf{r}, t) = n(\mathbf{r})\rho_{ge}(\mathbf{r}, t)e^{-i(k_0 z - \omega_0 t)}, \quad (15)$$

$$P_{gg'}(\mathbf{r}, t) = n(\mathbf{r})\rho_{gg'}(\mathbf{r}, t), \quad (16)$$

here we have factored out the concentration of atoms n .

To simplify the expressions and figure out the characteristic parameters of the problem, let us express the field variables in terms of the Rabi frequency

$$\Omega_s^{(\pm)}(\mathbf{r}, t) = \frac{d_0 D_s^{(\pm)}(\mathbf{r}, t)}{\hbar \varepsilon_0}, \quad (17)$$

where we introduce a reduced dipole moment d_0 [61]. In two-level systems, it can be the only transition dipole moment between the two considered states. If the degeneracy with respect to, for example, the magnetic quantum number m is important, d_0 is the part of the transition dipole moments independent of m . Since the transitions only happen between ground and excited states, the dipole matrix elements \mathbf{d}_{eg} (\mathbf{d}_{ge}) compose rectangular $N_e \times N_g$ ($N_g \times N_e$) matrices. Using d_0 , we can introduce dimensionless coefficients T_{egs} and T_{ges} , namely:

$$\mathbf{d}_{eg}\mathbf{e}_s = d_0 T_{egs}, \quad (18)$$

$$\mathbf{d}_{ge}\mathbf{e}_s^* = d_0 T_{ges},$$

so $T_{ges} = T_{egs}^*$. They can store the directional information and are proportional to Clebsch–Gordan coefficients. More details can be found in sec. III A. In the same way as \mathbf{d}_{eg} and \mathbf{d}_{ge} , T_{egs} and T_{ges} compose matrices of similar structure.

C. Equations within slowly-varying envelope and paraxial approximation

Performing rotating wave approximation for the regular part of (9) and applying similar approximations for the noise part, the equations for atomic variables take the form:

$$\frac{\partial}{\partial t} \rho_{ee'}(\mathbf{r}, t) = -i\Delta\omega_{ee'} \rho_{ee'}(\mathbf{r}, t) + i \sum_{g, s} \left(\Omega_s^{(+)}(\mathbf{r}, t) T_{egs} \rho_{ge'}(\mathbf{r}, t) - \Omega_s^{(-)}(\mathbf{r}, t) \rho_{eg}(\mathbf{r}, t) T_{ge's} \right), \quad (19)$$

$$\begin{aligned} \frac{\partial}{\partial t} \rho_{eg}(\mathbf{r}, t) = & -i\Delta\omega_{eg} \rho_{eg}(\mathbf{r}, t) - i \sum_s \Omega_s^{(+)}(\mathbf{r}, t) \left(\sum_{e'} \rho_{ee'}(\mathbf{r}, t) T_{e'gs} - \sum_{g'} T_{eg's} \rho_{g'g}(\mathbf{r}, t) \right) \\ & + \sum_{e', s} f_s^{(-)*}(\mathbf{r}, t) \rho_{ee'}(\mathbf{r}, t) T_{e'gs}, \end{aligned} \quad (20)$$

$$\begin{aligned} \frac{\partial}{\partial t} \rho_{ge}(\mathbf{r}, t) = & i\Delta\omega_{eg} \rho_{ge}(\mathbf{r}, t) + i \sum_s \Omega_s^{(-)}(\mathbf{r}, t) \left(\sum_{e'} T_{ge'e} \rho_{e'e}(\mathbf{r}, t) - \sum_{g'} \rho_{gg'}(\mathbf{r}, t) T_{g'es} \right) \quad (21) \\ & + \sum_{e', s} f_s^{(+)*}(\mathbf{r}, t) T_{ge'e} \rho_{e'e}(\mathbf{r}, t), \end{aligned}$$

$$\begin{aligned} \frac{\partial}{\partial t} \rho_{gg'}(\mathbf{r}, t) = & -i\Delta\omega_{gg'} \rho_{gg'}(\mathbf{r}, t) + i \sum_{e, s} \left(\Omega_s^{(-)}(\mathbf{r}, t) T_{ges} \rho_{eg'}(\mathbf{r}, t) - \Omega_s^{(+)}(\mathbf{r}, t) \rho_{ge}(\mathbf{r}, t) T_{eg's} \right) \\ & + \sum_{e, s} f_s^{(+)*}(\mathbf{r}, t) T_{ges} \rho_{eg'}(\mathbf{r}, t) + \sum_{e, s} f_s^{(-)*}(\mathbf{r}, t) \rho_{ge}(\mathbf{r}, t) T_{eg's}, \end{aligned} \quad (22)$$

for compactness, here we have omitted the pump and decay terms due to coefficients Γ_{ijkl} , detunings between atomic levels were denoted as

$$\Delta\omega_{ee'} = \omega_e - \omega_{e'} \quad (23)$$

$$\Delta\omega_{eg} = \omega_e - \omega_g - \omega_0 \quad (24)$$

$$\Delta\omega_{gg'} = \omega_g - \omega_{g'}. \quad (25)$$

By means of combining (3)-(8) into a wave equation for $\mathcal{D}(\mathbf{r}, t)$, using paraxial and rotating wave approximations in regular and noise parts, the equations for field propagation take the form

$$\left[\frac{\partial}{\partial z} + \frac{1}{c} \frac{\partial}{\partial t} - \frac{i}{2k_0} \left(\frac{\partial^2}{\partial x^2} + \frac{\partial^2}{\partial y^2} \right) + \left(\frac{\mu(\mathbf{r}, t)}{2} + i\delta(\mathbf{r}, t)k_0 \right) \right] \Omega_s^{(+)}(\mathbf{r}, t) = \\ i \frac{3}{8\pi} \lambda^2 \Gamma_{\text{rad.}} \left(n(\mathbf{r}) \sum_{e,g} T_{ges} \rho_{eg}(\mathbf{r}, t) + f_s^{(+)}(\mathbf{r}, t) \right), \quad (26)$$

$$\left[\frac{\partial}{\partial z} + \frac{1}{c} \frac{\partial}{\partial t} + \frac{i}{2k_0} \left(\frac{\partial^2}{\partial x^2} + \frac{\partial^2}{\partial y^2} \right) + \left(\frac{\mu(\mathbf{r}, t)}{2} - i\delta(\mathbf{r}, t)k_0 \right) \right] \Omega_s^{(-)}(\mathbf{r}, t) = \\ -i \frac{3}{8\pi} \lambda^2 \Gamma_{\text{rad.}} \left(n(\mathbf{r}) \sum_{g,e} \rho_{ge}(\mathbf{r}, t) T_{egs} + f_s^{(-)}(\mathbf{r}, t) \right), \quad (27)$$

here we have used the conventions (17), (18); the magnitude of transition dipole moment d_0 is represented via the spontaneous emission rate due to radiative transitions $\Gamma_{\text{rad.}} = \frac{\omega_0^3 d_0^2}{3\pi\varepsilon_0 \hbar c^3}$; the permittivity ε of the medium conditioned by mechanisms other than transition between considered atomic levels and is expressed via real part δ and imaginary part β related to absorption coefficient μ , namely $\varepsilon = (1 - \delta + i\beta)^2$, $\mu = 2k_0\beta$, both δ, β are assumed to be small quantities as is usually the case in x-ray domain.

Since the equations for the fields (26), (27) are linear, we can decompose $\Omega_s^{(\pm)}(\mathbf{r}, t)$ into two components characterized by two similar independent equations

$$\Omega_s^{(\pm)}(\mathbf{r}, t) = \Omega_{s, \text{det.}}^{(\pm)}(\mathbf{r}, t) + \Omega_{s, \text{noise}}^{(\pm)}(\mathbf{r}, t), \quad (28)$$

here $\Omega_{s, \text{det.}}^{(\pm)}(\mathbf{r}, t)$ are driven by the initial conditions and deterministic parts of equations (26) and (27) containing density matrix elements $\rho_{ge}(\mathbf{r}, t)$. Correspondingly, noise components $\Omega_{s, \text{noise}}^{(\pm)}(\mathbf{r}, t)$ are driven by the noise terms $f_s^{(\pm)}(\mathbf{r}, t)$.

D. The structure of the noise terms

Within the paraxial and rotating wave approximations, the noise terms in (19)-(22), (26)-(27) are obtained as projections of full vectorial noise from Eqs. (3)-(10) on unit polarization vectors

$$f_s^{(+)}(\mathbf{r}, t) = \mathbf{f}(\mathbf{r}, t) \mathbf{e}_s^*, \quad (29)$$

$$f_s^{(-)}(\mathbf{r}, t) = \mathbf{f}^\dagger(\mathbf{r}, t) \mathbf{e}_s. \quad (30)$$

Physically, the application of paraxial approximation assumes that the emission propagates along the z -axis. However, the emission also includes spontaneous photons that generally do not have any preferred direction and can break paraxial approximation. Mathematically, the spontaneous emission enters the equations at the level of the noise terms. In order to satisfy the conditions for the paraxial approximation, we have to exclude the Fourier components of the noise terms that do not belong to a given small solid angle Δo around the forward direction along the z -axis. Since the excluded spontaneous emission weakly interacts with the medium, it can be accounted on the level of Γ coefficients (9). The proposed procedure modifies the correlation properties (10) broadening the delta functions in the xy -plane. Now, the only non-zero correlators have the following form

$$\langle f_s^{(+)}(\mathbf{r}, t) f_{s'}^{(+)*}(\mathbf{r}', t') \rangle = \langle f_s^{(-)}(\mathbf{r}, t) f_{s'}^{(-)*}(\mathbf{r}', t') \rangle = F(\mathbf{r} - \mathbf{r}') \delta(t - t') \delta_{ss'}, \quad (31)$$

where $F(\Delta \mathbf{r})$ is the rest of the delta-function after truncating the neglected Fourier components

$$F(\mathbf{r}) = \frac{1}{(2\pi)^3} \int_{\Delta o} e^{i\mathbf{k}\mathbf{r}} d\mathbf{k} \approx \frac{\sin\left(\pi x \frac{\sqrt{\Delta o}}{\lambda}\right) \sin\left(\pi y \frac{\sqrt{\Delta o}}{\lambda}\right)}{\pi^2 xy} \delta(z - z'). \quad (32)$$

The integration over the \mathbf{k} -vectors within solid angle Δo gives a bell function with the waist $\sim \frac{\lambda}{\sqrt{\Delta o}}$.

Noise terms in Equations (19)-(22), (26)-(27) have a number of specific properties that enable correct description of the spontaneous emission. Consider the initial stage when there are no coherences neither fields. Under these conditions, the noise contribution for the coherences in Eqs. (20), (21) is non-zero when the excited states are populated. The absence of noise terms in Eqs. (19) for the excited states prevents the emission or self-amplification when the excited states are not populated. The noise contribution in Eqs. (22) for the ground

states is proportional to the coherences, thus becoming next-order contribution compared to the noise term for the coherences in Eqs. (20), (21). The noise terms for the field variables (26)-(27) are additive. However, due to correlation properties (31), only product of noise terms for the field and atomic variables have non-zero correlation. This enables us to recover the correct temporal profile of the emitted radiation in the limit of pure spontaneous emission, see further discussion in Sec. III.

E. Retarded time

For most of experimental realizations of x-ray superfluorescence, the time needed for the radiation to propagate along the axis of the medium is much longer than both the pump pulse duration and the decoherence time. Under these conditions, it is natural to introduce retarded time $\tau = t - z/c$ to avoid simulating large space-time domain where the pump is not present and – due to a rapid decay – no dynamics are observed. The change of variables of SPDE is intricate and should be done with care, a detailed derivation and discussion of involved approximations are given in Appendix A. Here, we only present the result of the transformation. Switching from old time variable t to retarded time τ

$$\Omega_s^{(\pm)}(\mathbf{r}, t = \tau + z/c) \rightarrow \Omega_s^{(\pm)}(\mathbf{r}, \tau), \quad (33)$$

the equations for the field variables (26), (27) drop the time derivatives

$$\left[\frac{\partial}{\partial z} - \frac{i}{2k_0} \left(\frac{\partial^2}{\partial x^2} + \frac{\partial^2}{\partial y^2} \right) + \left(\frac{\mu(\mathbf{r}, \tau)}{2} + i\delta(\mathbf{r}, \tau)k_0 \right) \right] \begin{pmatrix} \Omega_{s, \text{det.}}^{(+)}(\mathbf{r}, \tau) \\ \Omega_{s, \text{noise}}^{(+)}(\mathbf{r}, \tau) \end{pmatrix} = \quad (34)$$

$$i \frac{3}{8\pi} \lambda^2 \Gamma_{\text{rad.}} \begin{pmatrix} n(\mathbf{r}) \sum_{e, g} T_{ges} \rho_{eg}(\mathbf{r}, \tau) \\ f_s^{(+)}(\mathbf{r}, \tau) \end{pmatrix},$$

$$\left[\frac{\partial}{\partial z} + \frac{i}{2k_0} \left(\frac{\partial^2}{\partial x^2} + \frac{\partial^2}{\partial y^2} \right) + \left(\frac{\mu(\mathbf{r}, \tau)}{2} - i\delta(\mathbf{r}, \tau)k_0 \right) \right] \begin{pmatrix} \Omega_{s, \text{det.}}^{(-)}(\mathbf{r}, \tau) \\ \Omega_{s, \text{noise}}^{(-)}(\mathbf{r}, \tau) \end{pmatrix} = \quad (35)$$

$$- i \frac{3}{8\pi} \lambda^2 \Gamma_{\text{rad.}} \begin{pmatrix} n(\mathbf{r}) \sum_{g, e} \rho_{ge}(\mathbf{r}, \tau) T_{egs} \\ f_s^{(-)}(\mathbf{r}, \tau) \end{pmatrix}.$$

Before the transformations, $\Omega_{s, \text{noise}}^{(\pm)}(\mathbf{r}, t)$ were stochastic processes. Since the time derivatives disappear, the solution of the equations does not involve time integration of $f_s^{(\pm)}(\mathbf{r}, \tau)$, and fields $\Omega_{s, \text{noise}}^{(\pm)}(\mathbf{r}, \tau)$ remain noise function with the delta correlators in time

$$\langle \Omega_{s, \text{noise}}^{(+)}(\mathbf{r}_1, \tau_1) f_s^{(+)*}(\mathbf{r}_2, \tau_2) \rangle = i \frac{3}{8\pi} \lambda^2 \Gamma_{\text{rad.}} \delta(\tau_1 - \tau_2) \int G(\mathbf{r}_1 - \mathbf{r}) F(\mathbf{r} - \mathbf{r}_2) d\mathbf{r}, \quad (36)$$

$$\langle \Omega_{s, \text{noise}}^{(-)}(\mathbf{r}_1, \tau_1) f_s^{(-)*}(\mathbf{r}_2, \tau_2) \rangle = -i \frac{3}{8\pi} \lambda^2 \Gamma_{\text{rad.}} \delta(\tau_1 - \tau_2) \int G^*(\mathbf{r}_1 - \mathbf{r}) F(\mathbf{r} - \mathbf{r}_2) d\mathbf{r}, \quad (37)$$

where $G(\mathbf{r} - \mathbf{r}')$ is a Green function for equations (34). Note that it is convoluted with the paraxial correlator $F(\mathbf{r})$ from equation (32).

For the numerical implementation described in Appendix B, we discretized the equations using a split-step method. That is, the noise and deterministic parts of the fields will be integrated by means of different schemes. This is why we separate the fields (28) into two parts.

Similarly to the equations for the fields, the equations for the atomic variables (19)-(22) and properties of the noise terms (31) undergo transition to the retarded time $t \rightarrow \tau$. The atomic equations acquire additional terms when the noise terms are integrated in Ito's sense. These new terms can be interpreted as the incoherent terms containing Γ -coefficients (9) responsible for the spontaneous emission in the forward direction¹. The spontaneous emission in the other directions weakly interacts with the medium and can also be accounted on the level of Γ -terms², so the overall structure of the equations for the atomic variables remains unchanged (19)-(22).

F. Field correlation function

Once an ensemble of realizations of system evolution is calculated based on (19) – (22), (34), (35), observables of interest can be obtained following (1), (2). Most of the detectable x-ray observables of interest can be expressed via a field correlation function. In terms of the introduced Rabi-frequency notation (17) and ordinary time t , the field correlation function is expressed as

$$J_s(\mathbf{r}_1, \mathbf{r}_2, t_1, t_2) = \frac{\langle \Omega_s^{(+)}(\mathbf{r}_1, t_1) \Omega_s^{(-)}(\mathbf{r}_2, t_2) \rangle_{\text{trajectories}}}{\frac{3}{8\pi} \lambda^2 \Gamma_{\text{rad.}}}, \quad (38)$$

¹ The equations become sensitive to the integration method for the noise terms. Stratonovich integration generates even more terms with unclear physical meaning and is not suitable for the implementation of Euler-Murayama scheme discussed in Appendix B, so it will not be mentioned further in the article.

² More discussion can be found in sec. III B.

that is related to photon flux

$$\frac{dN_s^{(\text{ph.})}(\mathbf{r}, t)}{dtdS} = J_s(\mathbf{r}, \mathbf{r}, t, t). \quad (39)$$

Performing transition to retarded time τ (Appendix A), we have to recalculate the expression for the field correlation function (38). Since field variables $\Omega_s^{(\pm)}(\mathbf{r}, \tau)$ turn into noise terms, the choice of the integration method (Ito or Stratonovich) can introduce additional terms in equation (40). Independently of the chosen integration method, the expression (38) does not change its form for the case when $\tau_1 \neq \tau_2$

$$J_s(\mathbf{r}_1, \mathbf{r}_2, t_1 = \tau_1 + z_1/c, t_2 = \tau_2 + z_2/c) \rightarrow J_s(\mathbf{r}_1, \mathbf{r}_2, \tau_1, \tau_2) = \frac{\langle \Omega_s^{(+)}(\mathbf{r}_1, \tau_1) \Omega_s^{(-)}(\mathbf{r}_2, \tau_2) \rangle_{\text{trajectories}}}{\frac{3}{8\pi} \lambda^2 \Gamma_{\text{rad}}}, \quad (40)$$

However, the expression for the photon flux (39) corresponds exactly to the case when $\tau_1 = \tau_2$, when we have to introduce an additional term that corrects for the spontaneous emission contribution. To avoid it, we can just take the limit when $\tau_1 \rightarrow \tau_2$

$$\frac{dN_s^{(\text{ph.})}(\mathbf{r}, \tau)}{d\tau dS} = J_s(\mathbf{r}, \mathbf{r}, \tau', \tau)|_{\tau' \rightarrow \tau}. \quad (41)$$

For a numerical realization, two neighbouring time nodes can be used to estimate this limit.

G. Spontaneous emission within the stochastic methodology

The noise-terms in the equations of motion manifest themselves most prominently when considering the case of spontaneous emission. The evolution due to spontaneous emission can be modelled by assuming low atomic density $n(\mathbf{r})$, which lowers the chance of re-absorption of the spontaneously emitted photons. Practically, it means that we only leave the terms linearly dependent on $n(\mathbf{r})$ in equation (40). It still requires integration of the equations for the atomic variables. We neglect deterministic parts of the fields $\Omega_{s,\text{det.}}^{(\pm)}(\mathbf{r}, \tau)$ in (19) – (22), because they are proportional to $n(\mathbf{r})$. As a result, the equations become linear and can be straightforwardly integrated. Substituting the integrated expressions for the atomic coherences (20), (21) in the field equations (34), (35), and utilizing the correlation properties

(36), (37), we obtain

$$\begin{aligned}
J_s(\mathbf{r}_1, \mathbf{r}_2, \tau_1, \tau_2) &\approx \frac{3}{16\pi} \lambda^2 \Gamma_{\text{rad.}} e^{-\gamma_{\text{dec.}} |\tau_1 - \tau_2|} \\
&\times \int_{z < \min(z_1, z_2)} n(\mathbf{r}'_1) G(\mathbf{r}_1 - \mathbf{r}'_1) F(\mathbf{r}'_1 - \mathbf{r}'_2) G^*(\mathbf{r}_2 - \mathbf{r}'_2) \rho_s^{(\text{ex.})}(\mathbf{r}'_1, \min(\tau_1, \tau_2)) d\mathbf{r}'_1 d\mathbf{r}'_2 \\
&+ \mathbf{r}'_1 \leftrightarrow \mathbf{r}'_2, \quad (42)
\end{aligned}$$

where we have assumed that the coherences have a decay term corresponding to the decoherence time $\gamma_{\text{dec.}}$, $G(\mathbf{r})$ is Green's function for propagation of the emitted field. $\rho_s^{(\text{ex.})}(\mathbf{r}, \tau)$ stands for combination of atomic variables proportional to excited state populations. Analogously, we introduce a similar object for the ground state populations $\rho_s^{(\text{gr.})}(\mathbf{r}, \tau)$

$$\begin{aligned}
\rho_s^{(\text{ex.})}(\mathbf{r}, \tau) &= \sum_{e, e', g} T_{ges} \rho_{ee'}(\mathbf{r}, \tau) T_{e'gs}, \\
\rho_s^{(\text{gr.})}(\mathbf{r}, \tau) &= \sum_{g, g', e} T_{egs} \rho_{gg'}(\mathbf{r}, \tau) T_{g'es}.
\end{aligned} \quad (43)$$

The difference between these two values, namely the quantity $\rho_s^{(\text{ex.})}(\mathbf{r}, \tau) - \rho_s^{(\text{gr.})}(\mathbf{r}, \tau)$, can be interpreted as an effective population inversion.

H. Run-away trajectories and diffusion gauges

Besides the stability requirement of the numerical scheme of SPDE solution, the stochastic equations themselves should be free from solutions behaving like run-away trajectories [62], [63]. In [57], it has been shown that the freedom in construction of the noise-terms in compact systems can be used to suppress the divergent behaviour. This approach is easily extendable to the paraxial geometry. For each coordinate \mathbf{r} and retarded time τ corresponding to effective population inversion for any polarization s

$$\text{Re}(\rho_s^{(\text{ex.})}(\mathbf{r}, \tau)) > \text{Re}(\rho_s^{(\text{gr.})}(\mathbf{r}, \tau)) \quad (44)$$

we replace the density matrix elements in the equations for the field variables (34), (35) with their real parts

$$\begin{aligned}
\rho_{ge}(\mathbf{r}, \tau) &\rightarrow \frac{1}{2} (\rho_{ge}(\mathbf{r}, \tau) + \rho_{eg}^*(\mathbf{r}, \tau)), \\
\rho_{eg}(\mathbf{r}, \tau) &\rightarrow \frac{1}{2} (\rho_{eg}(\mathbf{r}, \tau) + \rho_{ge}^*(\mathbf{r}, \tau)).
\end{aligned} \quad (45)$$

³ In the stochastic formalism, the populations are complex, so we have to extract their real parts.

In accordance with generalized Girsanov theorem or drift gauge [62], [63], we have to re-weight the stochastic trajectories while averaging the observables (1), (2). Unfortunately, for a large number of atoms, this weight coefficient causes instabilities and worsens convergence, so we aim to neglect it. To compensate its absence, we reduce the need for the gauging by minimizing the difference between atomic variables $\rho_{eg}(\mathbf{r}, \tau)$ and $\rho_{ge}^*(\mathbf{r}, \tau)$. Since there is no unique way to define noise terms satisfying correlation properties (31), one can use this freedom to minimize average squared difference for each s , \mathbf{r} and τ

$$\left\langle \left| \sum_{eg} T_{ges} (\rho_{eg}(\mathbf{r}, \tau) - \rho_{ge}^*(\mathbf{r}, \tau)) \right|^2 \right\rangle, \quad (46)$$

reducing the difference between the sources in the equations for $\Omega_{\text{det.}}^{(+)}(\mathbf{r}, \tau)$ and $\Omega_{\text{det.}}^{(-)*}(\mathbf{r}, \tau)$. This freedom is typically referred as diffusion gauge.

The performance of this approximation for compact systems is analysed in [57]. In section IV B, we show that the modified equations reproduce correctly spontaneous emission – the seeding stage of the amplification process. The explicit form of the gauging functions can be found in Appendix B where we focus on the numerical realization.

III. IMPLEMENTATION FOR THE LEVEL SCHEME CORRESPONDING TO THE Cu- K_{α_1} TRANSITIONS

The expressions (19) – (22), (34) and (35) are general and can be applied to any superfluorescence problem where paraxial approximation is valid and the involved transitions are taking place predominantly between two groups of levels (excited and ground). For the numerical example, we will consider the level scheme corresponding to the strongest transition – K_{α_1} – of Cu atoms. In the context of XFEL experiments, the seeded amplified x-ray spontaneous emission on this transition was observed in [15], the Cu- K_{α_1} transition is a candidate for the first demonstration of the x-ray laser oscillator concept [20]. The technical details about numerical implementation can be found in Appendix B.

A. Terms required for Maxwell-Bloch part

The superfluorescence is initiated by an intense and focused pump pulse with x-ray photon energy above the ionisation threshold. As a result, the Cu atoms are transferred from ground

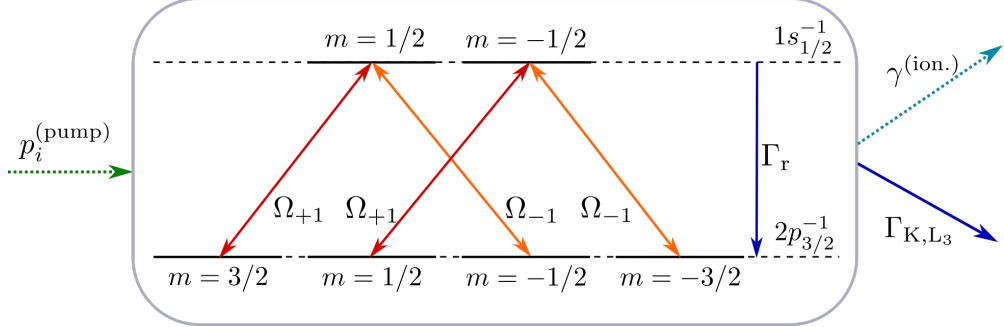


FIG. 1: Schematic representation of the $K\alpha_1$ system in copper. Excited states $1s_{1/2}^{-1}$ radiatively decay to $2p_{3/2}^{-1}$ states with spontaneous rate Γ_r , and are coupled by two radiation modes ($\Omega_{\pm 1}$). All ionic states are created by nonresonant photoionization from the atomic ground state ($p_i^{(\text{pump})}$), and can further decay spontaneously (Γ_K, Γ_{L_3}) or by photoionization with the pump and emitted fields ($\gamma^{(\text{ion.})}$).

state to core-ionized state, predominantly leaving the Cu atom in $1s_{1/2}^{-1}$ state. This state can decay radiatively to $2p^{-1}$ states or undergo other radiative as well as non-radiative channels, e.g. Auger-Meitner decay. We are interested in the strongest radiative channel, and thus will focus on $1s_{1/2}^{-1}$ to $2p_{3/2}^{-1}$ transition, that is, Cu- $K\alpha_1$ line. The considered level scheme is sketched in Fig. 1. To address the polarization properties of the emitted field, we have to explicitly treat the degenerate sublevels with different magnetic numbers. In terms of notation (12), the manifolds of excited and ground levels are

$$\begin{aligned} \mathbf{e} &= \left\{ 1s_{\frac{1}{2}, m=-\frac{1}{2}}, 1s_{\frac{1}{2}, m=\frac{1}{2}} \right\}, \\ \mathbf{g} &= \left\{ 2p_{\frac{3}{2}, m=-\frac{3}{2}}, 2p_{\frac{3}{2}, m=-\frac{1}{2}}, 2p_{\frac{3}{2}, m=\frac{1}{2}}, 2p_{\frac{3}{2}, m=\frac{3}{2}} \right\}. \end{aligned} \quad (47)$$

The tensor of dimensionless coefficients T_{ijs} for these levels can be calculated based on the Wigner-Eckart theorem (more in Appendix C 1). As a result, for the levels (47) we thus obtain

$$\left\{ T_{egs=1} \right\} = \begin{pmatrix} 2p_{\frac{3}{2}, m=-\frac{3}{2}} & 2p_{\frac{3}{2}, m=-\frac{1}{2}} & 2p_{\frac{3}{2}, m=\frac{1}{2}} & 2p_{\frac{3}{2}, m=\frac{3}{2}} \\ 0 & 0 & 1/3 & 0 \\ 0 & 0 & 0 & 1/\sqrt{3} \end{pmatrix} \begin{array}{l} 1s_{\frac{1}{2}, m=-\frac{1}{2}} \\ 1s_{\frac{1}{2}, m=\frac{1}{2}} \end{array} \quad (48)$$

$$\left\{ T_{egs=-1} \right\} = \begin{pmatrix} 2p_{\frac{3}{2},m=-\frac{3}{2}} & 2p_{\frac{3}{2},m=-\frac{1}{2}} & 2p_{\frac{3}{2},m=\frac{1}{2}} & 2p_{\frac{3}{2},m=\frac{3}{2}} \\ 1/\sqrt{3} & 0 & 0 & 0 \\ 0 & 1/3 & 0 & 0 \end{pmatrix} \begin{array}{l} 1s_{\frac{1}{2},m=-\frac{1}{2}} \\ 1s_{\frac{1}{2},m=\frac{1}{2}} \end{array} \quad (49)$$

here the index s – that describes polarization of the emitted field – takes the values $s = \{-1, 1\}$ corresponding to circular polarizations of the field. The remaining coefficients T_{ges} can be derived by conjugation, namely, $T_{ges} = T_{egs}^*$. The transitions corresponding to non-zero T_{egs} and T_{ges} are depicted on Fig.1. The analysis of possible transitions shows that the considered K_{α_1} level scheme can be presented as two Λ systems, namely composed of levels $\{2p_{\frac{3}{2},m=-\frac{3}{2}}, 1s_{\frac{1}{2},m=-\frac{1}{2}}, 2p_{\frac{3}{2},m=\frac{1}{2}}\}$ and $\{2p_{\frac{3}{2},m=\frac{3}{2}}, 1s_{\frac{1}{2},m=\frac{1}{2}}, 2p_{\frac{3}{2},m=-\frac{1}{2}}\}$. Each of the Λ systems interacts with fields of both polarization, as a result, in general case, neither field polarization modes or the Λ systems could be decoupled from one another.

B. Inclusion of the pump and decay processes

The equations (19) – (22) with levels associated according to (47) describe evolution only of small subsystem of atomic levels conditioned by interaction with resonance field only. This evolution should be coupled with multiple atomic processes – such as photoionization, Auger-Meitner decay, fluorescence, electron-impact ionisation, shake-off, and others – that follow the irradiation by an XFEL pulse [66]. In terms of equation (9), these processes are described by means of time- and space-dependent coefficients Γ_{ijkl} . Since the introduction of the retarded time and paraxial geometry only affects the structure of the equations for the field variables, we can directly include the terms with Γ coefficients (9) in equations (19)-(22) or their discrete analogs (B6) – (B9). For ASE description, an example of coupling a few-level-system MB-based formalism and a plasma-physics formalism – that describes the rest of the processes and provides the incoherent terms for the MB-like formalism – can be found in [67]. The evolution of the auxillary – with respect to equations (19) – (22) – levels can be described at the level of rate equations for level populations. Here, since we are not interested in atomic processes per se, we will limit ourselves to following the population only of the initial neutral state (that is needed to describe the pumping by photoionization) and a cumulative population of singly-ionized states non-resonant with $\text{Cu-}K_{\alpha_1}$ (that is needed to describe the absorption of the pump pulse). The resulting pump, decay, and decoherence

terms that we add to equations (19) – (22) have the following form

$$\frac{\partial}{\partial t} \rho_{ij}(\mathbf{r}, \tau)|_{\text{incoh.}} = -M_{ij}(\mathbf{r}, \tau) \rho_{ij}(\mathbf{r}, \tau) + \delta_{ij} \left(p_i^{(\text{pump})}(\mathbf{r}, \tau) + \Gamma_{\text{rad.}} \sum_k G_{ik}^{(\text{rad.})}(\mathbf{r}, \tau) \rho_{kk}(\mathbf{r}, \tau) \right), \quad (50)$$

here $M_{ij}(\mathbf{r}, \tau)$ describes decay and decoherence processes, $p_i^{(\text{pump})}(\mathbf{r}, \tau)$ describes pumping due to photoionization, $G_{ik}^{(\text{rad.})}(\mathbf{r}, \tau)$ describes radiative transitions between levels (47) conditioned by spontaneous isotropic fluorescence. The explicit form of these coefficients as well as further details on the implementation of incoherent processes, are discussed in Appendix C.

IV. NUMERICAL EXAMPLES AND DISCUSSION

In this section, we illustrate the x-ray emission modeling with the parameters close to the expected experimental conditions in XLO [20]. To provide sizeable population inversion using rapid photoionization, the XFEL pump pulse should have high pulse energy and be focused. To this aim, the assumed XFEL pulse energy is $250 \mu\text{J}$, the beam is focused down to $200 \text{ nm} \times 200 \text{ nm}$ FWHM, x-ray photon energy is 9 keV that is above the Cu K-edge. The temporal profile of the XFEL pulse is conditioned by the self-amplified spontaneous emission (SASE) process and is thus composed of a large number of randomly generated spikes [68]. However, here we would like to disentangle the stochasticity inherent in the current simulation approach from the SASE stochasticity, to this aim, we use a Gaussian temporal profile with 11.7 fs FWHM. As a medium that generates x-ray lasing, following [20], we consider a $270 \mu\text{m}$ thick jet of 8-molar solution of $\text{Cu}(\text{NO}_3)_2$ in water. We perform our calculations on a $900 \times 900 \text{ nm}$ spatial domain, with 64×64 grid points, with 40 grid points along the jet, and 180 points for the 37 fs long temporal domain.

A. Pump propagation

The key property that determines the dynamics of SF is population inversion. In its turn, it is determined by the dynamics of the pump pulse and the population of the ground (initial neutral) state. Fig. 2 shows the evolution of these quantities calculated according

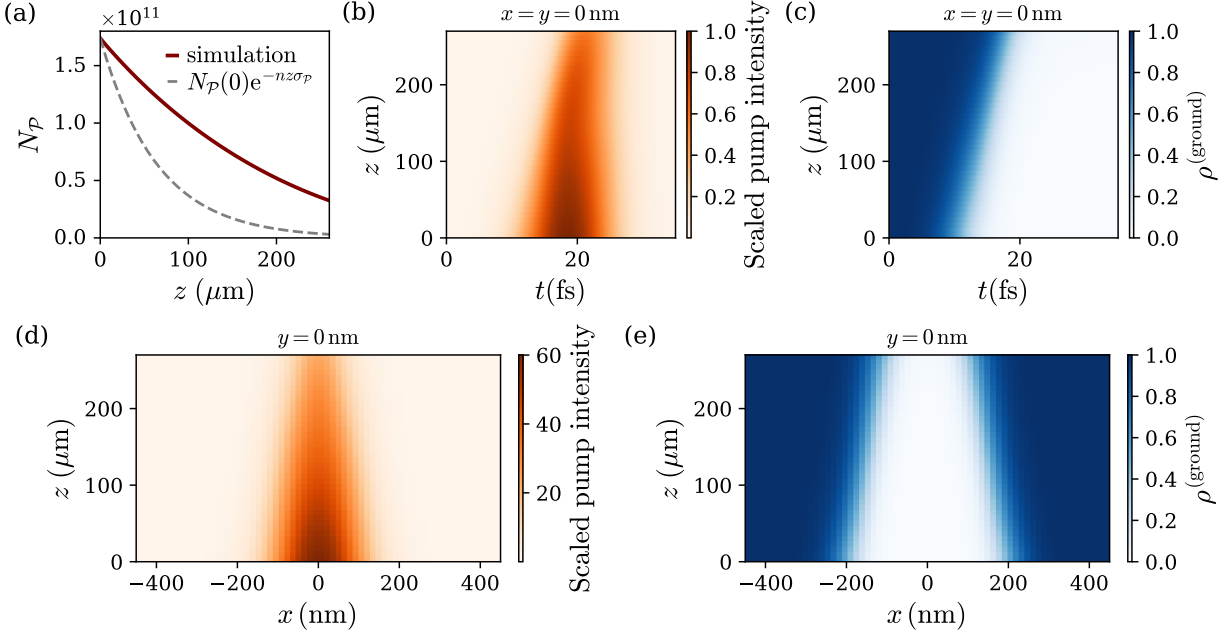


FIG. 2: (a) Number of pump photons as a function of propagation distance in the copper solution, the solid line denotes the numerical result of the simulation, and the dashed line denotes the number of photons obtained from the Beer-Lambert law; (b) spatio-temporal evolution of the pump field intensity and (c) ground state population along the target axis; longitudinal sections at $y = 0$ of (d) pump photon fluence (number of pump photons per unit area) and (e) population of the ground state after the end of the pump pulse.

to expressions from Appendix C. Fig. 2 (a) demonstrates strong bleaching – the number of pump photons drops significantly slower than it would according to Beer’s law, this phenomenon was studied at several FEL experiments [69], [70], [71]. Within our formalism, it is mostly conditioned by the decrease of the ground state population that has the largest absorption cross-section. Indeed, as Fig. 2 (c) shows, the population of the ground state drops to zero within the front part of the pump pulse. As a consequence, the front part of the pulse is absorbed more strongly than the tail part, resulting in shortening of the pulse and shifting its peak to later times – this behavior is observed in Fig. 2 (b). Recently, this shortening of the pulse was experimentally demonstrated [72] as well as modelled in detail based on collisional-radiative simulations [73]. Upon the propagation through the medium, the variation of the pump temporal profile is accompanied by the change of the transverse profile, see Fig. 2 (d). Since the bleaching effect is less pronounced for pulses of smaller

intensity, the outer parts of the pulse are absorbed more stronger than the central parts. Thus, the transverse size of the pump fluence shrinks upon propagation. As a result, upon propagation, the pump pulse decreases in energy, shrinks in size, as well as shrinks and delays in time. This behavior imprints on the population of the ground state of the atoms, see Fig. 2 (c) and (e). The product of the pump flux and initial neutral state population is the main contribution to the pumping rate $p_i^{(\text{pump})}$ in Eq.(50). This rate is the only inhomogeneous term in equations (19) – (22), (34) and (35), (50). Thus, the resulting non-uniform spatio-temporal pump and ground state distribution sets the stage for the SF emission analysed below.

B. Spontaneous emission

Before moving to the full SF simulation, let us consider the case of the spontaneous emission – a useful benchmark for our framework. The evolution due to spontaneous emission can be modelled by assuming low atomic density $n(\mathbf{r})$, which lowers the chance of re-absorption of the spontaneously emitted photons. Practically, it means that we neglect the deterministic source terms in the equations for the field (34), (35) or in their discrete analogs (B15), (B16). In this case, the evolution is completely conditioned by the noise terms, thus spontaneous emission case provides a useful benchmark for the developed formalism.

Fig. 3 compares the calculation of spontaneously emitted photon number based on expression (42) with the numerical simulation. For the simulation, parameters described in the beginning of Sec. (IV) were used. To simplify the analysis, the absorption of the emitted field was omitted. Every single realization (trajectory) results in photon numbers that show huge scatter. Moreover, the total emitted photon number – calculated based on (41) – takes negative as well as complex-valued values. This is expected from the structure of equations (34) and (35) – in the general case, the field variable representing the positive-frequency component $\Omega_s^{(+)}$ are not necessarily complex conjugate to the negative-frequency component $\Omega_s^{(-)}$. This is an inherent property of the developed approach, it is related to the way how the quantum-mechanical commutation relation of the field operators is reflected in the formalism. The resulting doubling of the number of field variables – that stems from treating the variables corresponding to amplitudes of positive and negative frequency components as independent complex numbers – is typical for phase-space methods based on positive-P

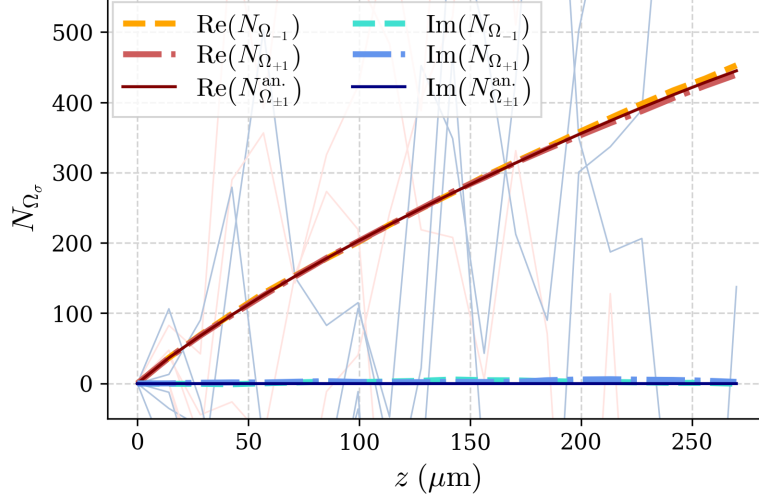


FIG. 3: Numerically (N_{Ω_σ}) and analytically ($N_{\Omega_\sigma}^{\text{an.}}$) calculated average number of emitted photons as function of propagation distance in Cu solution in the spontaneous emission approximation (see text). Thin lines denote examples of the real and imaginary part of the photon number for a single realization. The analytical solution is equal for both polarization modes, hence in the legend $s = \pm 1$. The amount of used stochastic realizations here and in Figs. 4, 5 is 10^5 .

representation, a deeper discussion can be found in [74]. However, single trajectories do not have a direct physical meaning – within the formalism, the value of quantum-mechanical observables is obtained based on averaging over an ensemble of trajectories. As Fig. 3 shows, after averaging over 10^5 trajectories, the imaginary part of photon numbers cancels out, and the real part agrees with the analytically calculated values.

The obtained shape of the dependence of spontaneously emitted photon number on the propagation distance z is a consequence of the Green's function behavior in paraxial approximation: For large distances z between points \mathbf{r} and \mathbf{r}' , the value of the Green's function is

$$|G(\mathbf{r} - \mathbf{r}')| = \frac{1}{\lambda z}. \quad (51)$$

Substitution of this limiting value in (41), (42) results in the following expression for the number of spontaneously emitted photons with polarization s traversing section S :

$$\frac{dN_s^{(\text{ph.})}}{d\tau} = \frac{3}{8\pi} \frac{S}{z^2} \Gamma_{\text{rad.}} \int n(\mathbf{r}) \rho_s^{(\text{ex.})}(\mathbf{r}, \tau) d\mathbf{r}. \quad (52)$$

The obtained expression shows expected behavior – the number of emitted photons is proportional to amount of excited atom within the volume and the solid angle S/z^2 within which the spontaneous radiation is collected. The pre-factor agrees with quantum-mechanical calculations based on Weisskopf–Wigner approximation [75], see also the discussion in [52].

For short propagation distance, Green's function turns into a delta-function

$$G(\mathbf{r} - \mathbf{r}') \approx \delta(\mathbf{r}_\perp - \mathbf{r}'_\perp), \quad (53)$$

meaning that the light travels almost parallel along the z -axis. Consequently, the number of spontaneously emitted photons with polarization s traversing the cross-section of the sample is

$$\frac{dN_s^{(\text{ph.,sp.})}}{d\tau} = \frac{3}{8\pi} \Delta o \Gamma_{\text{rad.}} \int n(\mathbf{r}) \rho_s^{(\text{ex.})}(\mathbf{r}, \tau) d\mathbf{r}. \quad (54)$$

The transition of asymptotic behaviour from (53) to (51) determines the dependence of the spontaneously emitted photon number on propagation distance: for small propagation distance, the dependence is linear since the Green's function (53) is constant; for larger propagation distance, the descending Green's function results in deceleration of the growth.

Fig. 4 shows field time-time correlation function integrated ⁴ over the simulation domain of the exit surface. The diagonal of the time-time correlation function describes the temporal profile of the emitted intensity, the width in the direction orthogonal to the diagonal describes the field temporal correlation properties. The averaging over stochastic realizations results in agreement between the numerically-calculated values and calculations based on analytical expression (42). The temporal profile of the emitted radiation is presented in Fig. 5 (a). Similarly to the case shown in Fig. 3, after averaging over trajectories, the imaginary part of the intensity cancels, and the real part agrees with the analytical expressions obtained from (42) and follows the population of the excited state. According to the Wiener–Khinchin theorem, the Fourier transform with respect to $\tau_1 - \tau_2$ provides the spectrum of the emitted

⁴ Since – within the spontaneous emission regime – the contribution from each voxel is conditioned by noise terms and is independent from other voxels, the transversely-integrated quantities require less trajectories to arrive at given S/N level compared to the case of quantities at given transverse coordinate x, y .

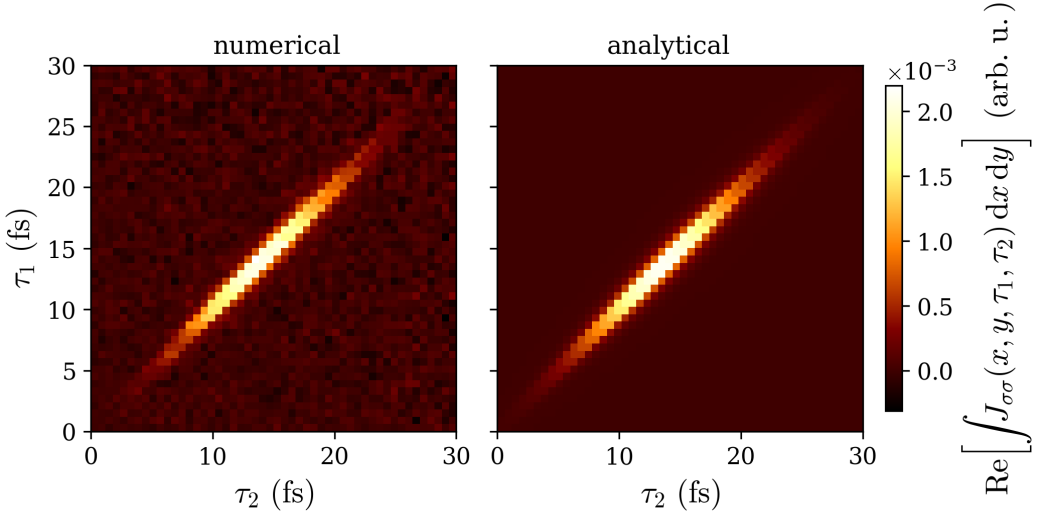


FIG. 4: Comparison of the numerically and analytically calculated field correlation function (40) at target exit integrated over transverse spatial directions x, y for $s = -1$.

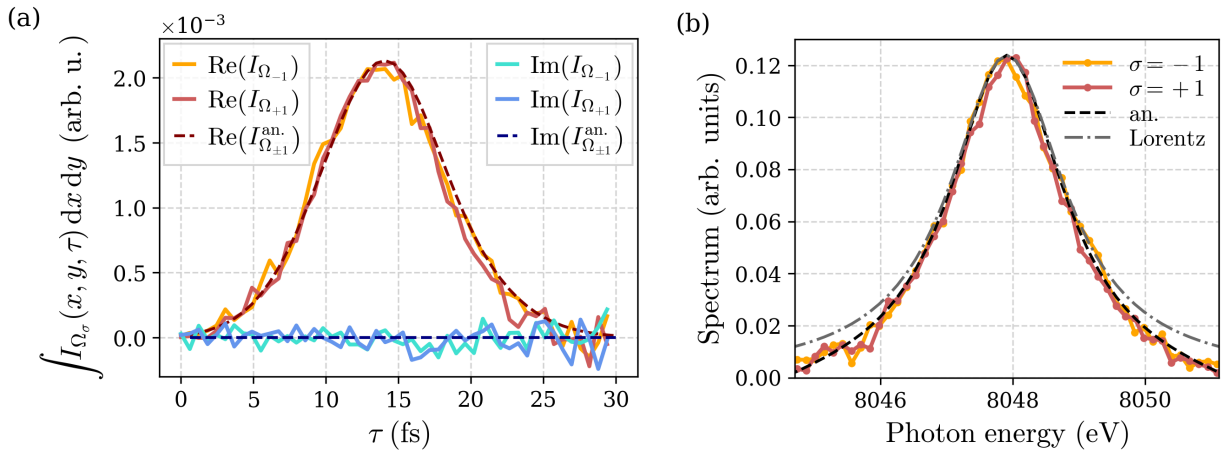


FIG. 5: (a) Temporal profile of field intensity emitted by the target exit integrated over transverse directions. (b) Numerically calculated spectrum of the two radiation modes emitted by the target exit, along with the spectrum calculated from the analytical field correlation function (an.)

radiation. Fig. 5 (b) shows the resulting spectrum, it agrees well with the analytical expression that is based on (42) and is close to Lorentzian profile with $\gamma_{\text{dec.}}$ HWHM. Also, as expected, Figs. (3) and (5) shows that properties of the spontaneously emitted radiation are independent from polarization.

The ability to reproduce the field correlation function (42) in the limit of spontaneous

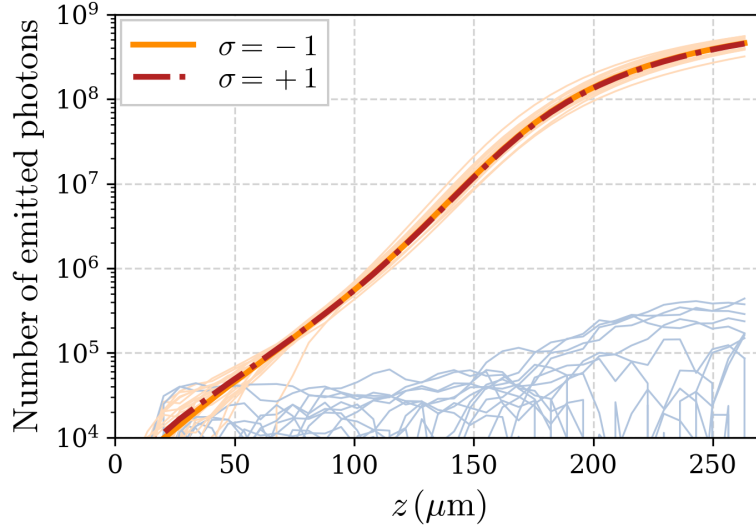


FIG. 6: Evolution of the total number of emitted photons with propagation distance z . Thin lines correspond to individual trajectories, orange color denotes the real part, blue – imaginary.

emission by means of the noise terms is a distinctive feature of the presented formalism compared to formalism [42] that uses phenomenologically-introduced noise terms. The agreement in both spectral and temporal profiles achieved here became possible thanks to non-trivial structure of the noise terms of the applied stochastic formalism.

C. Field evolution and transverse properties

The modeling of equations (19) - (22), (34), (35) augmented – in a self-consistent way – with pump propagation equations of Appendix C describes evolution of superfluorescence. Fig. 6 shows the number of emitted photons – calculated based on photon flux (40), (41) integrated over time and transverse simulation domain – as a function of propagation within medium. In the beginning of the medium, the evolution is conditioned by the spontaneous emission, and the noise terms have the key role. Here, similar to Fig. 3, individual trajectories show large scatter as well as comparable value of real and imaginary parts.

For larger propagation distances, approximately exponential growth of the emitted photon number takes place, this regime is typically referred to as ASE [76], [77], [78]. In this regime, the emitted field and coherences are still. As a result in the equations for evolution of the excited (19) and ground states (22) the terms proportional to field-coherence product can

be neglected. Then, the evolution of excited and ground states is conditioned by pump and decay terms only. Under this conditions, equations (20) - (21) become linear with time- and space-dependent coefficients. Considering for simplicity the case when the decoherence rate $\gamma_{\text{dec.}}$ is large, the produced linear response of coherences towards the field results in amplification with gain coefficient

$$\frac{3}{8\pi} n(\mathbf{r}) \lambda^2 \frac{\Gamma_{\text{rad.}}}{\gamma_{\text{dec.}}} (\rho_s^{(\text{ex.})}(\mathbf{r}, \tau) - \rho_s^{(\text{gr.})}(\mathbf{r}, \tau)). \quad (55)$$

Thanks to the modification of equations (34), (35) discussed in section II H, the combinations $\Omega_s^{(\pm)} + \Omega_s^{(\mp)*}$ are amplified with gain coefficient (55), while the combinations $\Omega_s^{(\pm)} - \Omega_s^{(\mp)*}$ do not have amplification term. As a result, the spurious imaginary part of photon-number observable does not grow in the ASE regime, as Fig. 6 shows.

The exponential-like growth of the photon number is limited by nonlinear effects. When the produced field and the generated coherences become large enough, the corresponding terms in (19), (22) cannot be neglected. As a result, the population inversion decreases and saturation sets in. Depending on the parameters of the system, the Rabi-oscillations kind of behavior may take place [52]. As Fig. 6 shows, some growth of the spurious imaginary part of photon-number observable takes place, however, it stays essentially smaller than the real part that has reached saturation. In both ASE and saturation regimes, the noise terms are smaller than the regular terms in equations (19) - (22), (34), (35). As a consequence, the scatter of the real part of the photon-number observable trajectories shows – upon propagation – approximately the same width in the log scale. This observation suggests that in the deep ASE and saturation regimes, within logarithmic accuracy, few trajectories could be used to obtain the expectation value of the photon-number observable.

The knowledge of transverse field distribution – and directly related to it angular distribution of the emitted intensity – are essential for various applications of SF. E.g., in [18] the larger angular spread of seeded-SF emission compared to the angular spread of the seed pulse enabled to detection of the seeded Mn K β signal. Another example where the angular properties of the SF radiation are crucial is XLO – in this case, the angular divergence determines the effectivity of the in-coupling of the SF radiation into the crystal cavity. Fig. 7 illustrates the properties related to transverse field distribution at propagation distances corresponding to the spontaneous emission (SE), ASE regime and to the saturation regime

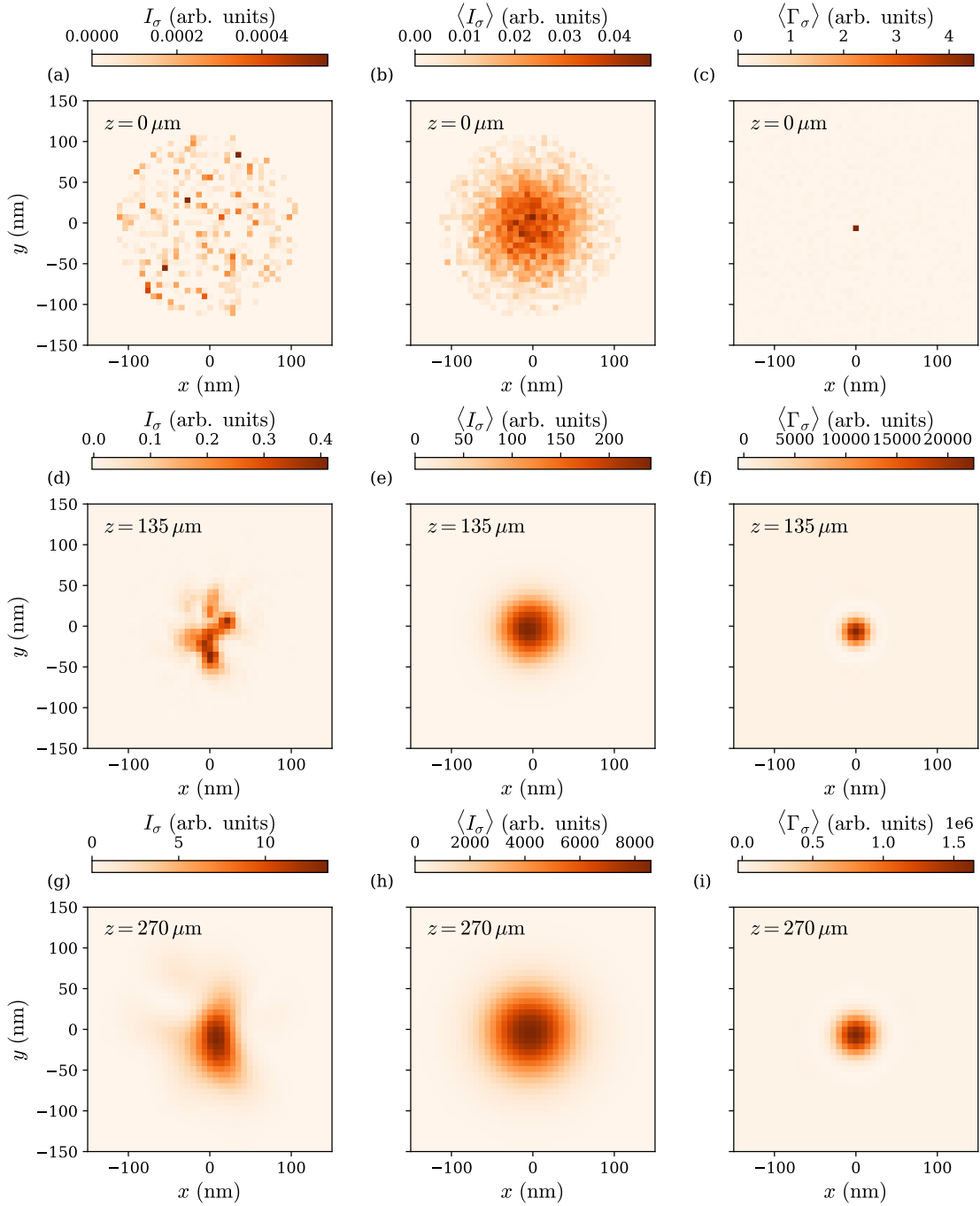


FIG. 7: Transverse field distribution: (a), (d), (g) intensity distribution of the emitted radiation for a single realization; (b), (e), (h) – the same quantity calculated by means of averaging over an ensemble of realizations; (c), (f), (i) – field correlation function in the transverse direction calculated according to Eq. (56). The row of figures (a)-(c), (d)-(f), and (g)-(i) correspond to a propagation distance of $z = 0 \mu\text{m}$ (SE regime), $z = 135 \mu\text{m}$ (ASE regime), and $270 \mu\text{m}$ (SF regime) and time $\tau_{\text{peak}} = 11 \text{ fs}$, 15 fs , and 17 fs respectively when the peak value of the intensity is observed. The number of numerical realizations is 20000 for the SE regime, and 1000 for ASE/SF respectively.

(superfluorescence regime, SF). Fig. 7 (a), (d), (g) shows intensity distribution for a single run of the numerical scheme (a single trajectory). In the case of SE, the spontaneously emitted intensity varies stochastically pixel to pixel, Fig. 7 (a). Upon propagation, due to the diffraction, the neighboring pixels establish correlation resulting in a speckle-like pattern. As Fig. 7 (d), (g) shows, the size of the speckles grows upon propagation. However, as it was discussed for Figs. 3, 6, a single realisation does not have a direct physical meaning – an ensemble of realisations is needed to describe the process of interest. The properties of the process are addressed by means of calculating the corresponding observables. In our case, one of the properties of interest is the transverse size of the emitted field. This property can be addressed by means of calculating the intensity, it is shown in Fig. 7 (b), (e), (h). Upon averaging over realizations, a smooth and axially-symmetric distribution comes out. Another property of interest is the transverse coherence of the emitted radiation. A rough estimate of this property can be obtained based on the size of the speckle. As an observable quantifying the transverse coherence property, we can consider the transverse correlation function [75]

$$\Gamma_s(\mathbf{r}_\perp, z, \tau) := \int \Omega_s^{(+)}(\mathbf{r}', z, \tau) \Omega_s^{(-)}(\mathbf{r}'_\perp + \mathbf{r}_\perp, z, \tau) d\mathbf{r}'_\perp. \quad (56)$$

Fig. 7 (c), (f), (i) shows this observable. As expected, the size of transverse correlation function approximately agrees with the size of the speckles. In particular, size of transverse correlation function starts with the size of just one pixel for the case of SE, Fig. 7 (c), and grows upon propagation. Since the transverse size of the correlation function is smaller than the transverse width of the intensity profile, the SF field is not fully transversely coherent – as also the speckle structure suggests. The ratio of the transverse width of the intensity profile to speckle size gives an estimate of the effective number of transverse modes.

The evolution of the transverse field profile is conditioned by the distribution of the population inversion as well as diffraction effects. Fig. 8 (a) shows the dependence of photon flux observable on propagation distance at several transverse positions. As expected, at the center of the beam the flux is largest and decreases towards the edge. This agrees with the distribution of the population inversion shown in Fig. 8 (b) for propagation distances corresponding to the entrance to the medium, ASE regime, and the saturation regime. The population inversion decreases with beam propagation due to pump absorption and

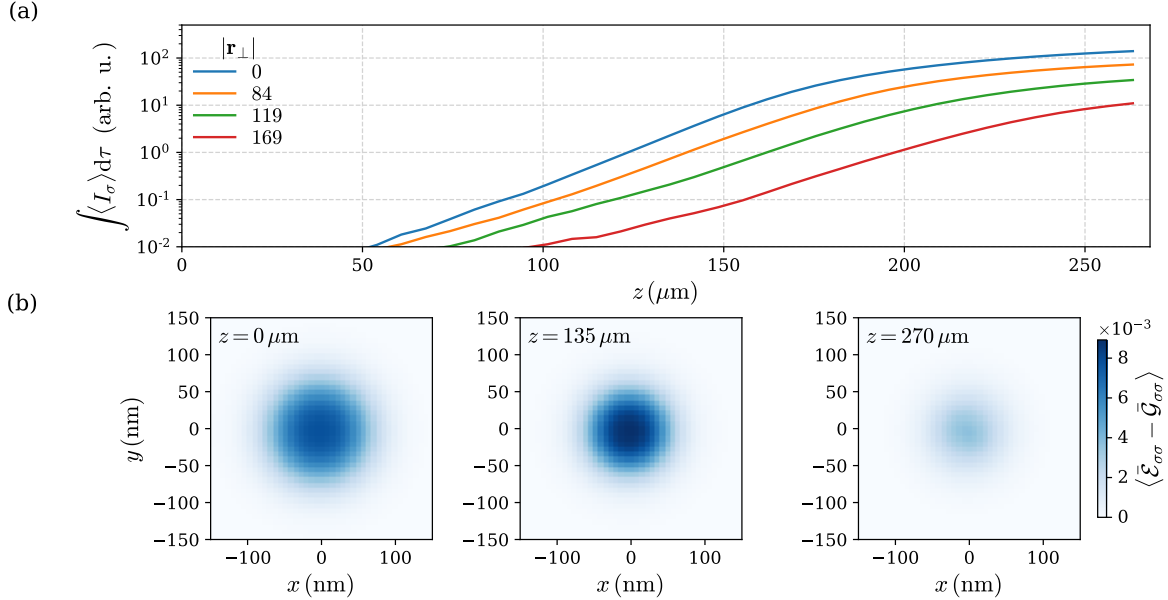


FIG. 8: (a) Emitted flux (time-integrated number of photons per unit area) as a function of propagation distance z for several positions in the transverse direction: on the axis ($\mathbf{r}_\perp = 0$ nm) and progressively further from the axis ($\mathbf{r}_\perp = 84, 119, 169$ nm); (b) Transverse cuts of the effective population inversion for propagation distances $z = 0, 135, 270 \mu\text{m}$.

nonlinear (saturation) effects. Within the ASE regime, a larger population inversion closer to the beam axis leads to larger amplification of the emitted radiation. As a result, the beam experiences gain guiding [79] and decreases in size. However, as Fig. 8 (a) shows, for the inner parts of the beam the transition from ASE to saturation takes place at a shorter propagation distance than for the outer parts. As a result, after the saturation regime sets in for the on-axis part of the beam, the beam size increases – as the middle column of Fig. 7 also illustrates.

D. Spectral-angular properties

The transverse and temporal profiles of the emitted x-ray field are hard to directly measure experimentally. Typically, x-ray fields are measured in far field, thus the angular distribution of the emitted intensity can be detected. To access the temporal properties of x-ray pulse, the crystal analyzers are typically used. E.g., in [16] the fringes in the observed x-ray spectrum were used to reconstruct the temporal separation between the peaks of the under-

lying field temporal profile. If a 2D detector is used to measure the field after the analyser crystal, the profile in the dispersive direction – a direction parallel to line along which the detector plane and the diffraction plane intersect – provides the spectral information, the profile in the non-dispersive direction – orthogonal to the dispersion direction – provides the angular information.

Fig. 9 (a) shows a spectral-angular distribution for a single realization at propagation distance z corresponding to the SE regime. As expected, it is isotropic in the angular direction and is highly noisy. Fig. 9 (d), corresponding to the ASE regime, shows several spikes that can be associated with the field modes that have emerged out of the spontaneous emission noise. Fig. 9 (g) shows a similar distribution at a larger propagation distance z corresponding to SF regime. It illustrates that the most intense modes are amplified further, and less intense modes fade out. This behavior is close to the mode clearance phenomena well-known in the FEL physics [80]. The tendencies observed on single-trajectory level are confirmed by spectral-angular intensity profiles averaged over an ensemble of realizations, Fig. 9 (b), (e), (h). Namely, the angular distribution is isotropic for the SE case, Fig. 9 (b), narrows down for ASE case shown Fig. 9 (e) and further decreases for the SF regime, Fig. 9 (h).

The temporal properties of the emitted field can be characterized by means of the field correlation function (40). A convenient way to analyse it is to represent it in terms of Wigner distribution:

$$W_s(\mathbf{r}_\perp, z, \omega, \tau) = \int d\tau' \langle \Omega_s^{(+)}(\mathbf{r}_\perp, z, \tau + \tau'/2) \Omega_s^{(-)}(\mathbf{r}_\perp, z, \tau - \tau'/2) e^{i\omega\tau'} \rangle. \quad (57)$$

The projection of the Wigner distribution on the time axis gives the intensity temporal profile, the projection on the frequency axis – the spectral profile. Fig 9 (c), (f), (i) shows Wigner distribution – calculate based on an ensemble of realizations – for propagation distance z corresponding to the SE, ASE and SF regime. The profile on time-axis is conditioned – to large extent – by the temporal profile of the population inversion present after the pump pulse. The profile on the frequency-axis is influenced by the decoherence rate of the transition. As a result, the spectral width of the produced radiation is broadened compared to the width determined by the emitted pulse duration, that is, the radiation is not transform-limited. If the radiation would be fully-coherent and the field amplitude would have a

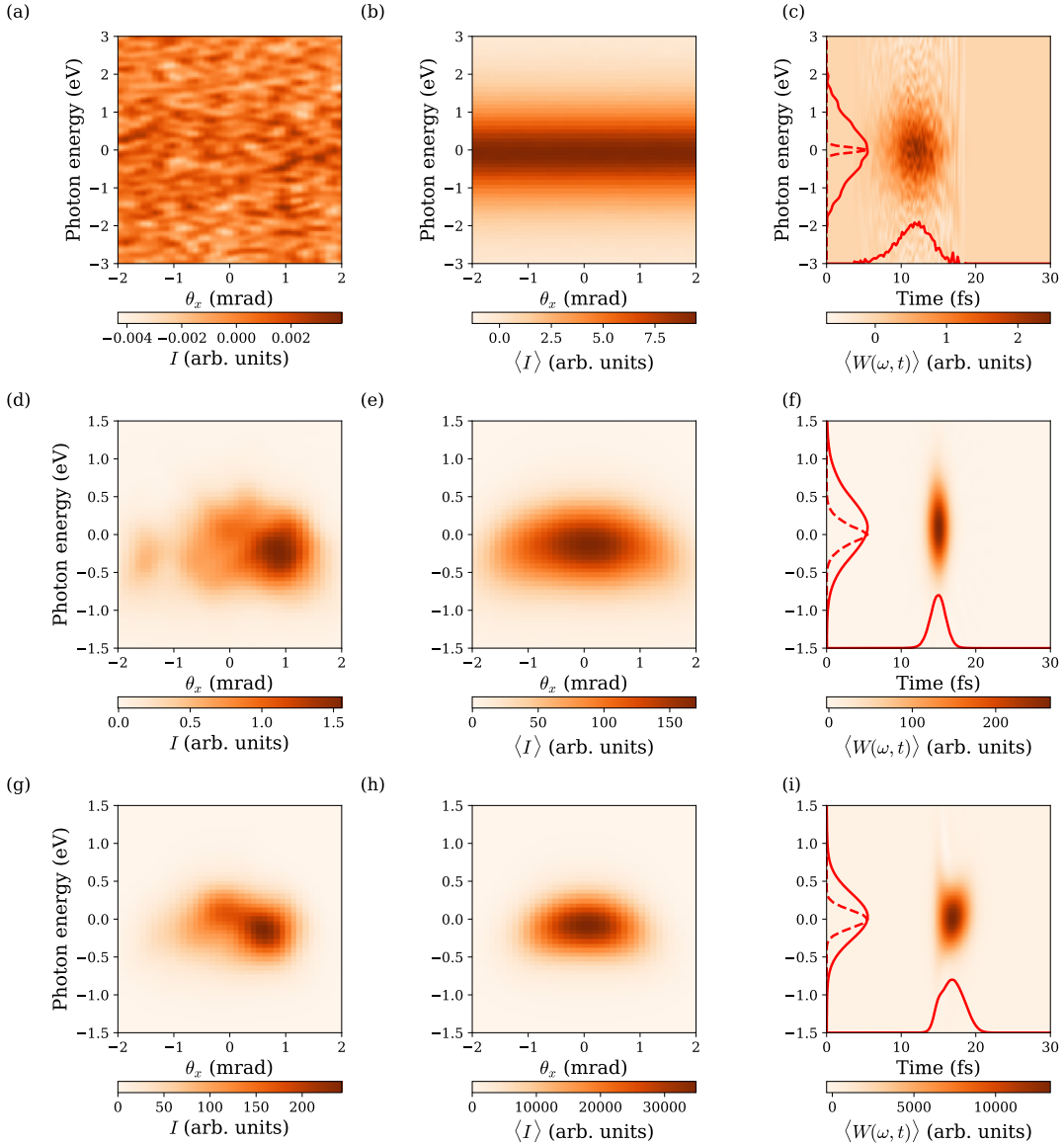


FIG. 9: Spectral-angular properties of the emitted radiation: (a), (d), (g) – spectral-angular distribution of the emitted radiation integrated over the θ_y direction for a single realization; (b), (e), (h) – same quantity calculated by means of averaging over an ensemble of realizations; (c), (f), (i) – Wigner distribution (57) at the center of the beam ($x = y = 0$), solid red lines show projections of the Wigner function onto the time and energy axis thus giving the temporal intensity profile and spectrum, dashed red line shows how the spectrum calculated according to (58) would look like. The row of figures (a)-(c), (d)-(f), and (g)-(i) correspond to propagation distance of $z = 0$ (SE regime), $z = 135 \mu\text{m}$ (ASE regime), and $z = 270 \mu\text{m}$ (SF regime). The number of numerical realizations is 1000 for the SE regime, and 100 for ASE/SF respectively.

constant phase, the connection between spectrum $I(\omega) = \int d\tau W(\omega, \tau)$ and intensity profiles $I(\tau) = \int d\omega W(\omega, \tau)$ due to transform-limited conditions would be expressed as:

$$\bar{I}(\omega) = \left| \int d\tau e^{i\omega\tau} \sqrt{I(\tau)} \right|^2. \quad (58)$$

The spectral profile $\bar{I}(\omega)$ calculated according to (58) is shown as dashed line on Fig 9 (c), (f), (i). As expected, since the emitted field is not transform-limited, it is narrower than the actual spectral profile. However, during the propagation, the spectral profile becomes narrower due to gain-narrowing effect that takes place in the ASE regime [77], as the comparison of Fig 9 (c) and (f) shows. Deep in the SF regime, the emitted fields may become so large that the induced dynamics – similar to Rabi oscillations – may cause additional broadening and splitting [53], in the presented example this regime is not pronounced.

E. Field polarization properties

The implemented 6-level scheme (47) of Cu-K $_{\alpha_1}$ transition – that treats the energy-degenerate levels that differ only in magnetic quantum number – enables one to address transitions caused by each of the field polarizations. Within this level scheme, the inner-level atomic coherences that are sensitive to the field polarization properties can be followed, e.g. the density matrix element $\rho_{2p_{\frac{3}{2}},m=-\frac{3}{2},2p_{\frac{3}{2}},m=\frac{1}{2}}$. As a result of the atomic 6×6 density matrix evolution, for each of the field polarization component a corresponding source due to induced atomic media polarization can be obtained, namely, the quantities

$$\begin{aligned} \mathcal{P}_s^{(+)}(\mathbf{r}, \tau) &= \sum_{e,g} T_{ges} \rho_{eg}(\mathbf{r}, \tau), \\ \mathcal{P}_s^{(-)}(\mathbf{r}, \tau) &= \sum_{e,g} \rho_{ge}(\mathbf{r}, \tau) T_{egs}, \end{aligned} \quad (59)$$

that enter the field equations (34), (35). In this way, equations (19) - (22), (34), (35) describe in self-consistent way the polarization properties of the emitted field and corresponding media polarization.

For a quantitative description of the field polarization state, we will use the field coherency matrix [81]

$$G_{\alpha\beta}^{(2)}(\mathbf{r}_\perp, z, \tau) = \langle \Omega_\alpha^{(+)}(\mathbf{r}_\perp, z, \tau) \Omega_\beta^{(-)}(\mathbf{r}_\perp, z, \tau) \rangle \quad (60)$$

and connect it to the Stokes parameters S_i , $i = 0, 1, 2, 3$ [81]:

$$G_{\alpha\beta}^{(2)}(\mathbf{r}_\perp, z, \tau) = \frac{1}{2} S_i(\mathbf{r}_\perp, z, \tau) \sigma_{\alpha\beta}^{(i)} \quad (61)$$

here $\sigma_{\alpha\beta}^{(i)}$ are Pauli matrices, indexes α, β take two values that denote polarization with respect to linear basis $\mathbf{e}_x, \mathbf{e}_y$ ⁵.

Fig. 10 (a), (d), (g) illustrates the polarization state of the field for a single realization.

⁵ The connection between the circular and linear basis is given by $\Omega_\alpha = M_{\alpha s} \Omega_s$, $M_{\alpha s} = \frac{1}{\sqrt{2}} \begin{pmatrix} 1 & -1 \\ i & i \end{pmatrix}$, $\alpha = x, y$, and $s = -1, +1$

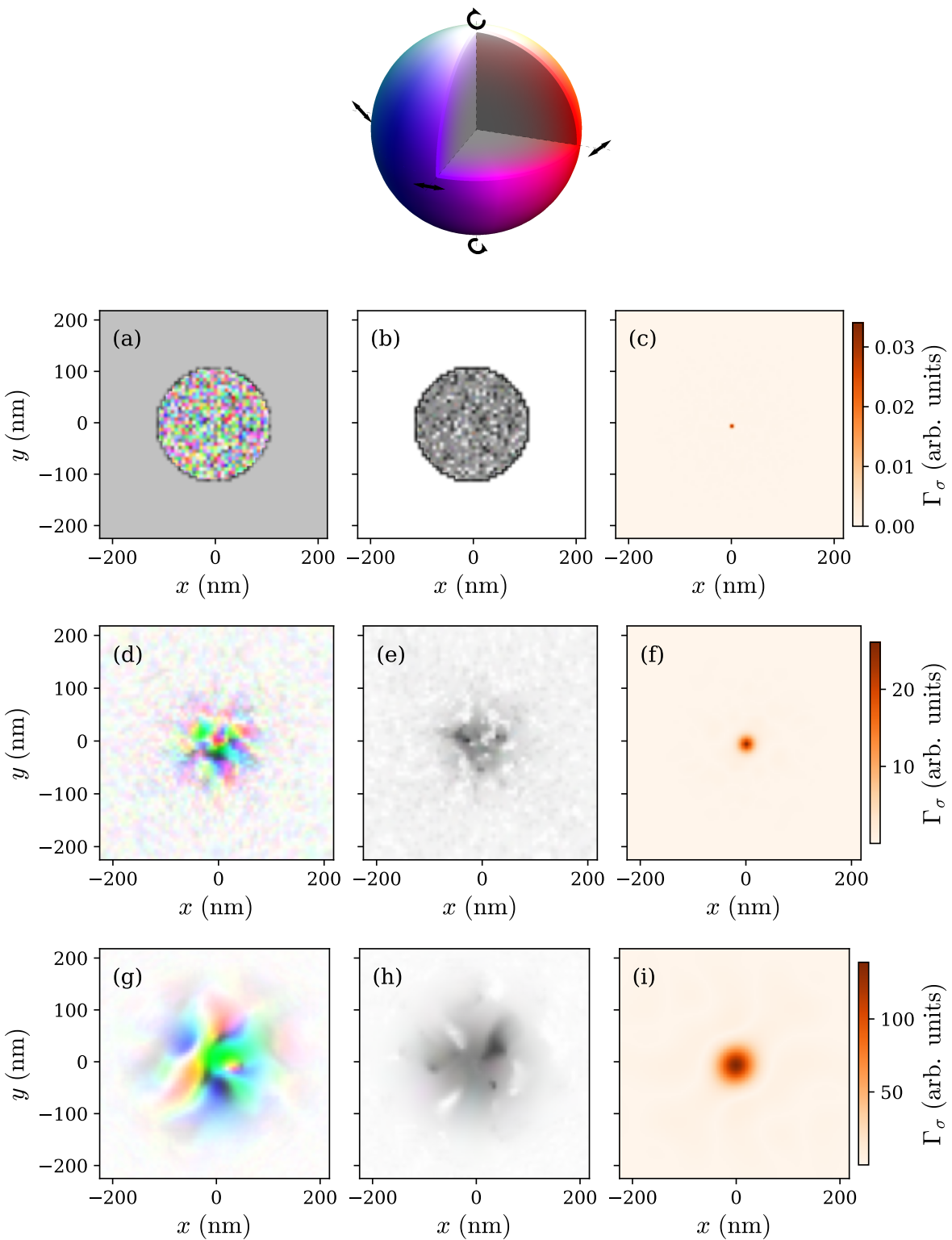


FIG. 10: Field polarization of the emitted radiation. Upper part: color-coding of polarization state described with help of Poincaré sphere construction. Hue, lightness, and saturation of the color depict longitude, the latitude on the Poincaré sphere, and polarization degree. In this way, saturated colors of varying hue – at the equator of the Poincaré sphere – denote linear polarization of correspondingly varying polarization direction, the black (white) color – at the south (north) pole of the Poincaré sphere – denotes left (right) circularly polarized light, the gray color – at the center of the Poincaré sphere – denote an unpolarized state of light. The general elliptic polarization states correspond to the surface of the Poincaré sphere and are denoted by saturated colors, the partially-polarized states correspond to the inner part of the Poincaré sphere and are denoted by partly-saturated colors. Lower part: (a), (d), (g) – transverse crosssection of polarization state for a single realization, (b), (e), (h) – transverse crosssection of polarization state calculated based on the ensemble of 50 realizations. The opacity of the color at a given point is proportional to the intensity of the radiation at that point; (c), (f), (i) – correlation of the polarization state quantified according to Eq.(63). The row of figures (a)-(c), (d)-(f), and (g)-(i) correspond to propagation distance of $z = 0$ (SE regime), $z = 135 \mu\text{m}$ (ASE regime), and $z = 270 \mu\text{m}$ (SF regime) and time $\tau_{\text{peak}} = 11 \text{ fs}$, 15 fs , and 17 fs respectively.

The polarization state is encoded via color: we use the Poincaré sphere [81] to describe the polarization state, the longitude and latitude on the Poincaré sphere are encoded in the hue and the lightness of the color, correspondingly, the degree of polarization is encoded by the saturation of the color, the opacity of the color is proportional to the intensity of the radiation. For a single realization, the emitted field is close to be fully polarized, the polarization state changes randomly from speckle to speckle. This behaviour can be observed in figs. 10 (a), (d), (g) as the appearance of saturated colorful speckles. Fig. 10 (b), (e), (h) shows the polarization state obtained from the field coherency matrix averaged over an ensemble of realizations. As expected, the emitted field is on average unpolarized, this is seen in fig. 10 (b), (e), (h) where the gray color signifies that the radiation has polarization degree close to zero. This behaviour agrees with the 1D analysis presented in [82], where it was concluded that the single shots of the emitted SF radiation are fully polarized but with

a random polarization direction. However, in our case, in contrast to the 1D case, there are several spatial modes, thus the polarization direction is varying within the transverse cross-section.

The speckles of colors observed in figs. 10 (a), (d), (g) point towards correlation of the field polarization properties between neighboring points in the transverse cross-section. To quantify this kind of correlation, let us consider 4-th order moment of the field taken in two points in space:

$$G_{\alpha\beta\gamma\delta}^{(4)}(\mathbf{r}_\perp, \mathbf{r}'_\perp, z, \tau) = \langle \Omega_\alpha^{(+)}(\mathbf{r}_\perp, z, \tau) \Omega_\beta^{(-)}(\mathbf{r}_\perp, z, \tau) \Omega_\gamma^{(+)}(\mathbf{r}'_\perp, z, \tau) \Omega_\delta^{(-)}(\mathbf{r}'_\perp, z, \tau) \rangle, \quad (62)$$

and based on it construct a following observable:

$$C(\mathbf{r}_\perp, z, \tau) = \sum_{i,\alpha,\beta,\gamma,\delta} \int d\mathbf{r}'_\perp \frac{\sigma_{\alpha\beta}^{(i)} \sigma_{\gamma\delta}^{(i)} G_{\alpha\beta\gamma\delta}^{(4)}(\mathbf{r}'_\perp, \mathbf{r}'_\perp + \mathbf{r}_\perp, z, \tau)}{\sum_{\alpha',\beta'} G_{\alpha'\alpha'}^{(2)}(\mathbf{r}'_\perp, z, \tau) G_{\beta'\beta'}^{(2)}(\mathbf{r}'_\perp + \mathbf{r}_\perp, z, \tau)}. \quad (63)$$

For a classical light field, the expression under the integral gives a scalar product of two vectors on the Poincaré sphere, each of the vectors describe the polarization state of light at points \mathbf{r}'_\perp and $\mathbf{r}'_\perp + \mathbf{r}_\perp$ correspondingly. In this way, the quantity $C(\mathbf{r}_\perp, z, \tau)$ describes the proximity of polarization state at two points separated by a distance \mathbf{r}_\perp in the transverse direction. The quantity $C(\mathbf{r}_\perp, z, \tau)$ is shown in Figs. 10 (c), (f), (i). As expected for a quantity averaged over ensemble of realizations, $C(\mathbf{r}_\perp, z, \tau)$ is azimuthally-symmetric. By construction, the width in transverse direction \mathbf{r}_\perp of the quantity $C(\mathbf{r}_\perp, z, \tau)$ reflects the average size of the coherent region (speckle) within which the polarization properties of the radiation are close. As Figs. 10 (a), (c); (d), (f) and (g), (i) show, the extent of $C(\mathbf{r}_\perp, z, \tau)$ indeed reflects the size of the speckle observed in single realizations. Similarly to dynamics observed in Fig. 7, the size of the coherent region starts from a single pixel for SE regime and grows upon propagation, as comparison of Figs. 10 (c), (f), (i) shows.

F. Gain medium polarization properties and atomic coherences

The properties of the emitted field discussed above can be directly related to the experimentally measurable detector counts. In addition to these quantities, the numerical modeling

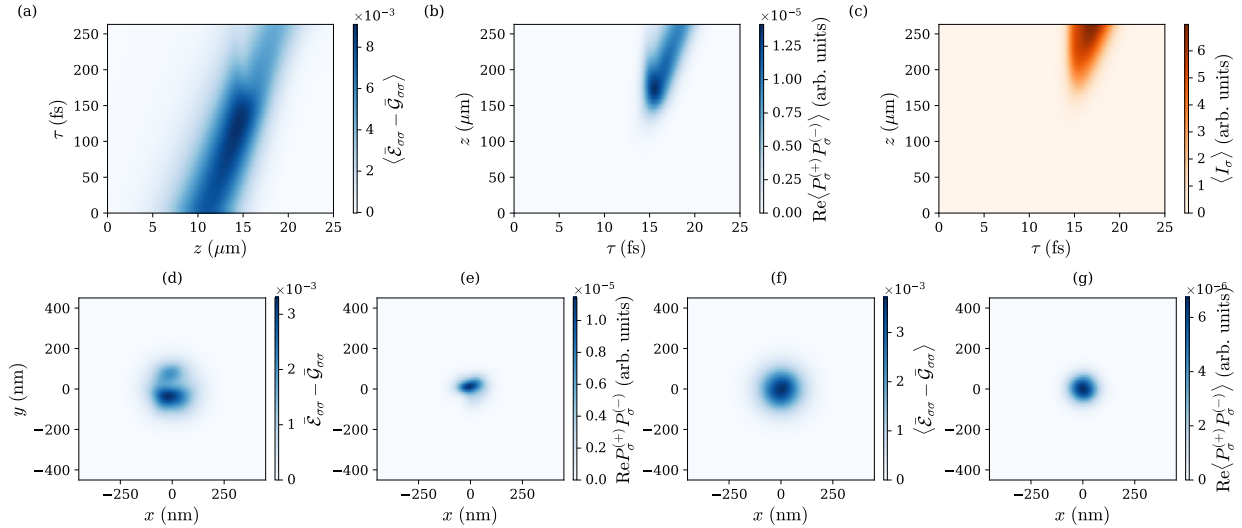


FIG. 11: Spatio-temporal evolution on the axis ($x = y = 0$) of (a) effective population inversion, (b) two-particle correlation between atomic coherences, and (c) emitted radiation intensity; transverse profiles for a single realization at propagation distance $z = 270$ μm and corresponding $\tau_{\text{peak}} = 17$ fs of (d) effective population inversion and (e) two-particle correlation between atomic coherences; (f), (g) – same quantities as (d), (e) but calculated based on an ensemble average of numerical realizations.

can provide atomic-system-related observables that are not straightforwardly measurable. As an example, consider an atomic property that is directly related to the field emission, namely polarization (59) that is proportional to atomic coherences. Similarly to the field amplitude, averaging over realizations results in $\langle \mathcal{P}_s^{(\pm)}(\mathbf{r}, \tau) \rangle = 0$ – even so for each individual trajectory the polarization has smooth and macroscopic behaviour, the averaging over random phase originating from noise terms results in nullifying. Concurrently, similarly to the field intensity, the quantity $\langle \mathcal{P}_s^{(+)}(\mathbf{r}, \tau) \mathcal{P}_s^{(-)}(\mathbf{r}, \tau) \rangle$ is not zero and describes the two-particle correlation between atomic coherences within voxel with center at point \mathbf{r} . Fig. 11 (b) shows the evolution of this quantity on axis with propagation through the medium. It goes through – similarly to field intensity shown in Fig. 11 (c) and Figs. 6, 8 – the amplification and saturation stages. In the saturation stage, Figs. 11 (a), (b) show faint oscillations that can be interpreted as Rabi oscillations. As expected for this case, their appearance overlaps with the increase of intensity shown in Fig. 11 (c). In the course of the oscillations, the decrease in the effective population inversion $\rho_s^{(\text{ex.})}(\mathbf{r}, \tau) - \rho_s^{(\text{gr.})}(\mathbf{r}, \tau)$ for the considered 6-level system (47) is accompanied with increase in two-particle correlation between atomic

coherences $\mathcal{P}_s^{(+)}\mathcal{P}_s^{(-)}$ – similarly to Bloch-vector length conservation for two-level systems. This anticorrelation between the effective population inversion and coherences is also visible in the transverse profile, Figs. 11 (d), (e).

V. CONCLUSIONS AND OUTLOOK

The general approach to quantum electromagnetic field - an ensemble of multilevel atoms interaction based on stochastic trajectories [55], [56], [57] was applied to a particular case of x-ray SF initiated by strongly focused XFEL pump pulses. The properties of this system allowed a number of simplifying approximations, such as: description based on slowly-varying envelope functions, paraxial approximation, and neglecting back-propagating wave. Under these assumptions, a system of SPDE was obtained (19) - (22), (34), (35) that has structure of MB equations augmented with the noise terms for both field and atomic variables. A numerical scheme (B6) - (B9), (B15) (B16) was proposed to model the resulting SPDE. Analysis presented in Sec. B and IV B shows that the noise terms of the SPDE are able to reproduce the temporal and spectral properties of the spontaneous emission in the forward direction – the critical quantum phenomenon that triggers ASE, and SF evolution. Augmenting the SPDE with PDE that describe the evolution of the XFEL pump pulse and population of certain atomic levels, a realistic description – including pumping, decay and decoherence – of the x-ray SF process was achieved. Based on ensemble of SPDE realizations, an extensive characterisation of the SF process can be performed by means of calculating corresponding observables, as illustrated in the Sec. IV.

The developed numerical approach can be used for designing and analyzing the x-ray SF experiments. The tensorial formulation of the basic equations enables straightforward extension to more complex level schemes. In this way, an extension to the necessary number of levels in the numerical scheme could be used as a solid basis for interpretation of sXES data [17], [18]. The ability to address the transverse properties of the emitted radiation could be used to interpret complex correlated pattern in non-dispersive and dispersive directions observed in [16], and thus improve the understanding and perform optimization of x-ray pulse pairs production.

In the context of modeling the XLO setup [20], the developed numerical scheme provides the necessary information about spectral, angular and polarization properties needed to

model the in-coupling of the x-ray SF radiation burst into the Bragg-crystal cavity. For the radiation that has made one trip within the cavity, the ability of the numerical scheme to describe the cross-over from spontaneous to stimulated emission would enable the determination of the lower threshold needed for the circulated radiation to overcome the spontaneous emission. Investigating the parameter space of the medium geometry and pump properties, the optimal conditions for obtaining bright and coherent x-ray pulses could be determined, and will be a subject of future publications.

ACKNOWLEDGMENTS

A.H. acknowledges the support of the U.S. Department of Energy Contract No. DE-AC02-76SF00515 and the resources provided by the National Energy Research Scientific Computing Center (NERSC), a U.S. Department of Energy Office of Science User Facility located at Lawrence Berkeley National Laboratory, operated under Contract No. DE-AC02-05CH11231 using NERSC award ERCAP0020725. S.K. acknowledges the research programme No. P1-0112, the research projects No. J1-8134 and PR-08965 of the Slovenian Research Agency, and the SLING consortium for providing computing resources of the HPC system NSC at the Jožef Stefan Institute. S.C. acknowledges the financial support of Grant-No. HIDSS-0002 DASHH (Data Science in Hamburg-Helmholtz Graduate School for the Structure of the Matter).

Appendix A: Transition to the retarded time

For K- α transitions in period-IV elements, the transient core-shell population inversion state – created by the pump pulse – relaxes on a fs timescale due to Auger-Meitner effect and x-ray fluorescence. As a result, the temporal range when non-trivial evolution of atomic variables occurs is conditioned mostly by the pump pulse duration. For typical media that are of interest for us – such as solution jets and solid samples – the typical thickness of the medium is $\sim 100 \mu\text{m}$, while the pump length $\sim c 10 \text{ fs} \sim 3 \mu\text{m}$. Under these conditions, using retarded time $\tau = t - z/c$ would select the relevant temporal range where most of dynamics takes place, and thus save computational resources. The transformation to the retarded time requires the change of variables in SDEs. Since the noise terms are not

smooth functions that could have been differentiated, change of variables should be done with caution.

1. Equivalence of Ito and Stratonovich forms and their differences

Consider SDE for a vectorial stochastic variable $\mathbf{x}(t)$ in the Ito form:

$$\frac{dx_i(t)}{dt} = A_i(\mathbf{x}, t) + \sum_j B_{ij}(\mathbf{x}, t) f_i(t). \quad (\text{A1})$$

Here $f_i(t)$ are normalized Gaussian white noise terms

$$\langle f_i(t) f_j(t') \rangle = \delta_{ij} \delta(t - t'). \quad (\text{A2})$$

The stochastic Ito equation can be related to the following finite difference scheme

$$\Delta x_i^{(t)} = A_i^{(t)} \Delta t + \sum_j B_{ij}^{(t)} \varepsilon_j^{(t)} \sqrt{\Delta t}, \quad (\text{A3})$$

where $\varepsilon_j^{(t)}$ are normalized Gaussian random numbers. By derivation [55], [56], the SDEs (3) - (10) and their paraxial analogs (19) – (22), (26) and (27) are in the Ito form with respect to time variable t . Note, that these equations involve complex noise terms in contrast to the examples given in this subsection. The complex noise term $f_{\text{com.}}(t)$ can be expressed through two real noise terms

$$f_{\text{com.}}(t) = \frac{1}{\sqrt{2}}(f_1(t) + i f_2(t)).$$

The convenience of the Ito form lies in the ease of the numerical implementation. According to the Ito interpretation (A3), the stochastic integration requires a new independent random contribution every time increment and involves dynamic variables from the previous time step. In contrast, the Stratonovich interpretation admixes the dynamic variables from the future

$$\Delta x_i^{(t)} = \bar{A}_i^{(t)} \Delta t + \frac{1}{2} \sum_j \left(B_{ij}^{(t)} + B_{ij}^{(t+1)} \right) \varepsilon_j^{(t)} \sqrt{\Delta t}, \quad (\text{A4})$$

Note, that the Stratonovich integration requires recalculation [83] of drift coefficients $\bar{A}_i(\mathbf{x}, t)$

$$\bar{A}_i(\mathbf{x}, t) = A_i(\mathbf{x}, t) - \frac{1}{2} \sum_{k,j} B_{kj}(\mathbf{x}, t) \frac{\partial}{\partial x_k} B_{ij}(\mathbf{x}, t), \quad (\text{A5})$$

One can show that equations (19) – (22), (26) and (27) do not acquire any additional terms when going from the Ito to Stratonovich formulation.

Fortunately, if the Stratonovich form of SDE is used, usual calculus laws remain valid [83]. Consequently, to simplify the change of variables, it is more convenient to work temporarily with the Stratonovich integration.

2. Properties of delta-functions involved in expressions for noise correlation

From the derivation of eqs. (3) - (10) presented in [56], it follows that there is a subtle difference between space and time delta-functions in equations (10) or their paraxial analogs (32). The derivation of spatial correlation properties requires continuous-medium description of atomic ensemble and electromagnetic field decomposition into modes. The delta-function in space $\delta(z - z')$ should be understood as a limiting value of a narrow distribution. The temporal delta correlation properties just signifies Ito or Stratonovich formulation of stochastic differential equations in time.

3. Transition to the retarded time

We aim to perform transformation

$$\tau = t - z/c. \quad (\text{A6})$$

The change of variables modifies the form of the differential equations. Replacing variables (t, z) with (τ, z) results into the following changes in the differentiation

$$\frac{\partial}{\partial t} \rightarrow \frac{\partial}{\partial \tau}, \quad c \frac{\partial}{\partial z} \rightarrow c \frac{\partial}{\partial z} + \frac{\partial}{\partial \tau}.$$

They are applicable even for the stochastic differential equations, if the Stratonovich representation is used.

As concluded in the previous subsection, the equations (19) – (22), (26) and (27) have exactly the same form in terms of Ito and Stratonovich noise terms. First, we temporarily assume the Stratonovich interpretation to perform transformation (A6). Then, the final equations will be transformed back to the Ito form in terms of retarded time τ .

The change of variables completely removes the time derivative from the equations for the field variables (34) and (35). The time differentiation only remains in the equations for the atomic variables (19) – (22).

Now, let us have a look at the transformation of the correlation properties (31). Since the transformation involves only two variables z and t , we ignore the correlations in the xy -plane

$$\begin{aligned} \langle f_s^{(\pm)}(\mathbf{r}, t) f_{s'}^{(\pm)*}(\mathbf{r}', t') \rangle &\sim \delta^{(\varepsilon)}(z - z') \delta(t - t') \delta_{ss'} \\ &= \delta^{(\varepsilon)}(\tau - \tau') \delta(c(\tau - \tau') + z - z') \delta_{ss'}. \end{aligned} \quad (\text{A7})$$

Here, ε is the finite waist of the corresponding delta function. Note that the broadened coordinate correlator has become a function of the retarded-time difference. It means that the time integration of the stochastic equations does not have Ito neither Stratonovich interpretation. To restore stochastic Ito equations, let us analyse the noise contributions to equations (19) – (22). Since the broadened noise terms are multiplied by the other dynamic variables, they create non-zero deterministic correlations that do not disappear in the limit of $\varepsilon = 0$. If we take them into account explicitly, we can safely consider $\varepsilon = 0$ and use the Ito interpretation for the time integration. For example, consider the noise contribution in equation (20) for density matrix elements $\rho_{eg}(\mathbf{r}, \tau)$

$$\begin{aligned} -i \sum_s \Omega_{s, \text{noise}}^{(+)}(\mathbf{r}, \tau) &\left(\sum_{e'} \rho_{ee'}(\mathbf{r}, \tau) T_{e'gs} - \sum_{g'} T_{eg's} \rho_{g'g}(\mathbf{r}, \tau) \right) \\ &+ \sum_{e', s} f_s^{(-)*}(\mathbf{r}, \tau) \rho_{ee'}(\mathbf{r}, \tau) T_{e'gs}. \end{aligned} \quad (\text{A8})$$

Let us shift atomic variables in time

$$\rho_{ij}(\mathbf{r}, \tau) = \rho_{ij}(\mathbf{r}, \tau - \varepsilon) + \int_{\tau-\varepsilon}^{\tau} \frac{\partial \rho_{ij}(\mathbf{r}, \tau')}{\partial \tau} d\tau', \quad (\text{A9})$$

so we can isolate $\rho_{ij}(\mathbf{r}, \tau - \varepsilon)$ that is not correlated with the noise terms anymore. Anything that creates correlations in (A8) is now localized in the integral in equation (A9)

$$\begin{aligned} -i \sum_s \int_{\tau-\varepsilon}^{\tau} \Omega_{s, \text{noise}}^{(+)}(\mathbf{r}, \tau) &\left(\sum_{e'} \frac{\partial \rho_{ee'}(\mathbf{r}, \tau')}{\partial \tau} T_{e'gs} - \sum_{g'} T_{eg's} \frac{\partial \rho_{g'g}(\mathbf{r}, \tau')}{\partial \tau} \right) d\tau' \\ &+ \sum_{e', s} \int_{\tau-\varepsilon}^{\tau} f_s^{(-)*}(\mathbf{r}, \tau) \frac{\partial \rho_{ee'}(\mathbf{r}, \tau')}{\partial \tau} T_{e'gs} d\tau'. \end{aligned} \quad (\text{A10})$$

The only unneglectable contribution here comes from the noise terms. The deterministic part of $\frac{\partial \rho_{ij}(\mathbf{r}, \tau')}{\partial \tau}$ cannot compensate smallness of the integral in the limit $\varepsilon = 0$. Since ε can be arbitrarily small, we can consider the cumulative effect of (A10) over time $\Delta T = N\varepsilon$ that is still small. If N is big, we can apply the central limit theorem and replace (A10) with its average

$$\left\langle -i \sum_s \int_{\tau-\varepsilon}^{\tau} \Omega_{s, \text{noise}}^{(+)}(\mathbf{r}, \tau) \left(\sum_{e'} \frac{\partial \rho_{ee'}(\mathbf{r}, \tau')}{\partial \tau} T_{e'gs} - \sum_{g'} T_{eg's} \frac{\partial \rho_{g'g}(\mathbf{r}, \tau')}{\partial \tau} \right) d\tau' + \sum_{e', s} \int_{\tau-\varepsilon}^{\tau} f_s^{(-)*}(\mathbf{r}, \tau) \frac{\partial \rho_{ee'}(\mathbf{r}, \tau')}{\partial \tau} T_{e'gs} d\tau' \right\rangle. \quad (\text{A11})$$

Applying correlation properties (A7), one gets spontaneous emission terms

$$-\frac{3}{16\pi} \Gamma_r \Delta o \sum_{g', e', s} T_{eg's} T_{g'e's} \rho_{e'g} \quad (\text{A12})$$

that can be included at the level of Γ coefficients (9). Similar result is obtained for the other equations for the atomic variables. The contribution proportional to $\rho_{ij}(\mathbf{r}, \tau - \varepsilon)$ gives Ito noise terms in the limit $\varepsilon = 0$ and correlation properties (A7) can be rewritten in the following way

$$\langle f_s^{(\pm)}(\mathbf{r}, \tau) f_{s'}^{(\pm)*}(\mathbf{r}', \tau') \rangle \sim \delta(\tau - \tau') \delta(z - z') \delta_{ss'}. \quad (\text{A13})$$

Note that $\delta(z - z')$ corresponds to the Stratonovich integration. For the Stratonovich interpretation the noise delta correlators can be seen as the limit of finite correlators, so the new total correlator (A13) does not differ from the one used before the change of variables (31).

Appendix B: Numerical realization

1. Noise terms, atomic and field variables on a grid

For the current implementation, we use a uniform rectangular grid with step size $\Delta x, \Delta y, \Delta z, \Delta \tau$ and follow the atomic and field variables at grid nodes denoted by a four-dimensional index $\mathbf{xyz}\tau$

$$\rho_{ij}(\mathbf{r}, \tau) \rightarrow \rho_{ij, \mathbf{xyz}\tau}, \quad \Omega_s^{(\pm)}(\mathbf{r}, \tau) \rightarrow \Omega_{s, \mathbf{xyz}\tau}^{(\pm)} \quad (\text{B1})$$

The noise contributions are modelled with the help of Gaussian random numbers with correlation properties

$$\langle \xi_{s,\mathbf{xyz}\tau}^{(\pm)} \xi_{s',\mathbf{x}'\mathbf{y}'\mathbf{z}'\tau'}^{(\pm)*} \rangle = \delta_{ss'} \delta_{\mathbf{xx}'} \delta_{\mathbf{yy}'} \delta_{\mathbf{zz}'} \delta_{\tau\tau'}, \quad (\text{B2})$$

that could be directly used to discretize the noise terms

$$f_s^{(\pm)}(\mathbf{r}, \tau) \rightarrow \frac{\xi_{s,\mathbf{xyz}\tau}^{(\pm)} + \xi_{s,\mathbf{xy}(\mathbf{z}+1)\tau}^{(\pm)}}{2\sqrt{\Delta z \Delta x \Delta y \Delta \tau}}, \quad f_s^{(\pm)*}(\mathbf{r}, \tau) \rightarrow \frac{\xi_{s,\mathbf{xyz}\tau}^{(\pm)*}}{\sqrt{\Delta z \Delta x \Delta y \Delta \tau}}. \quad (\text{B3})$$

Here, $f_s^{(\pm)}(\mathbf{r}, \tau)$ is represented by a sum of two discrete random numbers to restore broadened correlations between $f_s^{(\pm)}(\mathbf{r}, \tau)$ and $f_s^{(\pm)*}(\mathbf{r}, \tau)$ along z -axis (see the discussion below equation (10)). Although the paraxial correlator (32) has the finite waist in the xy -plane, broadening along the x - and y -axis is not necessary. If distances between neighbouring nodes on a grid match the waist of $F(\mathbf{r})$

$$\Delta o = \frac{\lambda^2}{\Delta x^2} = \frac{\lambda^2}{\Delta y^2},$$

the broadening effect of the paraxial correlator can be fully reproduced solely by the Green's function from the final discrete equations. In other words, the span of transverse wavevectors that can be addressed with a grid size Δx is $2\pi/\Delta x$, which exactly covers a solid angle equal to Δo . For typical wavelengths λ and grid sizes Δx used in practice, the solid angle Δo remains a small quantity.

2. Diffusion gauges

In section II H, we proposed to use the drift gauges for removing run-away realizations from the stochastic differential equations. The rigorous application of the drift gauges requires re-weighting trajectories from the final statistical sample. We aim to skip the re-weighting procedure. To mitigate the effect of this approximation, we employ the gauge freedom (sec. II H) to minimize the difference between atomic variables $\rho_{eg}(\mathbf{r}, \tau)$ and $\rho_{ge}^*(\mathbf{r}, \tau)$ and consequently minimize the effect of transformation (45). Note that correlation properties (B2) do not change under the following transformation

$$\begin{aligned} \xi_{s,\mathbf{xyz}\tau}^{(\pm)} &\rightarrow \xi_{s,\mathbf{xyz}\tau}^{(\pm)} \sqrt{\frac{16\pi g_{s,\mathbf{xyz}\tau}}{3\lambda^2 \Gamma_{\text{rad.}} \Delta z}}, \\ \xi_{s,\mathbf{xyz}\tau}^{(\pm)*} &\rightarrow \xi_{s,\mathbf{xyz}\tau}^{(\pm)*} \sqrt{\frac{3\lambda^2 \Gamma_{\text{rad.}} \Delta z}{16\pi g_{s,\mathbf{xyz}\tau}}}. \end{aligned} \quad (\text{B4})$$

To find suitable gauging coefficients $g_{s,\mathbf{xyz}\tau}$, we minimize expression (46) with respect to them. If we neglect coherences $\rho_{ee'}(\mathbf{r}, \tau)$ and $\rho_{gg'}(\mathbf{r}, \tau)$, coefficients $g_{s,\mathbf{xyz}\tau}$ can be expressed through the discretized version of $\rho_s^{(\text{ex.})}(\mathbf{r}, \tau)$ and $\rho_s^{(\text{gr.})}(\mathbf{r}, \tau)$ from equation (43)

$$g_{s,\mathbf{xyz}\tau} = \frac{\rho_{s,\mathbf{xyz}\tau}^{(\text{ex.})}}{\rho_{s,\mathbf{xyz}\tau}^{(\text{ex.})} - \rho_{s,\mathbf{xyz}\tau}^{(\text{gr.})}}. \quad (\text{B5})$$

Including $\rho_{ee'}(\mathbf{r}, \tau)$ and $\rho_{gg'}(\mathbf{r}, \tau)$ in equation (B5) would require more recalculations and is less practical. The neglected inter-level coherences are not created during the pump stage, they are developed during the interaction with the SF field. Since the noise terms are important at the spontaneous emission and ASE stages when no strong SF field is yet developed, the accounting for inter-level coherences for noise-terms calculation would be – at considered stages – a small correction compared to levels' populations.

3. Numerical scheme for the atomic variables

We use an approach similar to split-step method, and treat the increment of the regular part of the equations for atomic variables with suitable explicit high order algorithm, while for the noise part we use an explicit Euler-Murayama scheme

$$\rho_{ij,\mathbf{xyz}(\tau+1)} = \rho_{ij,\mathbf{xyz}\tau} + \Delta\rho_{ij,\mathbf{xyz}\tau}|_{\text{det.}} + \Delta\rho_{ij,\mathbf{xyz}\tau}|_{\text{noise.}}$$

In the present article, the time integration of the regular part of the atomic variables is performed separately for each \mathbf{xyz} -point with Runge-Kutta 4-th order algorithm

$$\frac{\Delta\rho_{ee',\mathbf{xyz}\tau}}{\Delta\tau}|_{\text{det.}} = \left[-i\Delta\omega_{ee'}\rho_{ee'} + i\sum_{g,s} \left(\Omega_{s,\text{det.}}^{(+)} T_{egs}\rho_{ge'} - \Omega_{s,\text{det.}}^{(-)} \rho_{eg} T_{ge's} \right) \right]_{\text{RK, xyz}\tau} \quad (\text{B6})$$

$$\frac{\Delta\rho_{eg,\mathbf{xyz}\tau}}{\Delta\tau}|_{\text{det.}} = \left[-i\Delta\omega_{eg}\rho_{eg} - i\sum_s \Omega_{s,\text{det.}}^{(+)} \left(\sum_{e'} \rho_{ee'} T_{e'gs} - \sum_{g'} T_{eg's} \rho_{g'g} \right) \right]_{\text{RK, xyz}\tau} \quad (\text{B7})$$

$$\frac{\Delta\rho_{ge,\mathbf{xyz}\tau}}{\Delta\tau}|_{\text{det.}} = \left[i\Delta\omega_{eg}\rho_{ge} + i\sum_s \Omega_{s,\text{det.}}^{(-)} \left(\sum_{e'} T_{ge's} \rho_{e'e} - \sum_{g'} \rho_{gg'} T_{g'es} \right) \right]_{\text{RK, xyz}\tau} \quad (\text{B8})$$

$$\frac{\Delta\rho_{gg',\mathbf{xyz}\tau}}{\Delta\tau}|_{\text{det.}} = \left[-i\Delta\omega_{gg'}\rho_{gg'} + i\sum_{e,s} \left(\Omega_{s,\text{det.}}^{(-)} T_{ges}\rho_{eg'} - \Omega_{s,\text{det.}}^{(+)} \rho_{ge} T_{eg's} \right) \right]_{\text{RK, xyz}\tau} \quad (\text{B9})$$

Note that the equations only contain the deterministic fields $\Omega_{s,\text{det.}}^{(\pm)}(\mathbf{r}, \tau)$. The interaction with the noise parts of the fields $\Omega_{s,\text{noise}}^{(\pm)}(\mathbf{r}, \tau)$ must be taken into account together with the

other noise terms at the level of Euler-Murayama scheme

$$\frac{\Delta\rho_{ee',xyz\tau}}{\Delta\tau}\Big|_{\text{noise}} = i\sum_{g,s}\left(\Omega_{s,\text{noise}}^{(+)}T_{egs}\rho_{ge'} - \Omega_{s,\text{noise}}^{(-)}\rho_{eg}T_{ge's}\right)_{xyz\tau} \quad (\text{B10})$$

$$\begin{aligned} \frac{\Delta\rho_{eg,xyz\tau}}{\Delta\tau}\Big|_{\text{noise}} &= \sum_s \left[i\Omega_{s,\text{noise}}^{(+)} \left(\sum_{g'} T_{eg's}\rho_{g'g} - \sum_{e'} \rho_{ee'}T_{e'gs} \right) + \right. \\ &\quad \left. \sqrt{\frac{\gamma g_s^{-1}}{2\Delta\tau}} \xi_s^{(-)*} \sum_{e'} \rho_{ee'}T_{e'gs} \right]_{xyz\tau} \end{aligned} \quad (\text{B11})$$

$$\begin{aligned} \frac{\Delta\rho_{ge,xyz\tau}}{\Delta\tau}\Big|_{\text{noise}} &= \sum_s \left[i\Omega_{s,\text{noise}}^{(-)} \left(\sum_{e'} T_{ge's}\rho_{e'e} - \sum_{g'} \rho_{gg'}T_{g'es} \right) + \right. \\ &\quad \left. \sqrt{\frac{\gamma g_s^{-1}}{2\Delta\tau}} \xi_s^{(+)*} \sum_{e'} T_{ge's}\rho_{e'e} \right]_{xyz\tau} \end{aligned} \quad (\text{B12})$$

$$\begin{aligned} \frac{\Delta\rho_{gg',xyz\tau}}{\Delta\tau}\Big|_{\text{noise}} &= \sum_{e,s} \left[i \left(\Omega_{s,\text{noise}}^{(-)} T_{ges}\rho_{eg'} - \Omega_{s,\text{noise}}^{(+)} \rho_{ge}T_{eg's} \right) + \right. \\ &\quad \left. \sqrt{\frac{\gamma g_s^{-1}}{2\Delta\tau}} (\xi_s^{(+)*}T_{ges}\rho_{eg'} + \xi_s^{(-)*}\rho_{ge}T_{eg's}) \right]_{xyz\tau} \end{aligned} \quad (\text{B13})$$

Here, we have already performed the transformation (B4) and introduced the gauging function $g_{s,xyz\tau}$ from equation (B5). For brevity, we have also introduced effective an radiative decay rate

$$\gamma = \frac{3}{8\pi} \frac{\lambda^2}{\Delta x \Delta y} \Gamma_{\text{rad.}} = \frac{3}{8\pi} \Delta o \Gamma_{\text{rad.}} \quad (\text{B14})$$

Consequently, the coefficient γ defines the proportion of the spontaneous emission participating in the amplification process. This coefficient turns out to be a universal constant further appearing in the equations for the discrete field variables.

4. Numerical scheme for the field variables

Given the atomic variables at grid nodes $\rho_{ij,xyz\tau}$, we can propagate the field variables using multislicing approach [64], [65]. To simplify the differentiation along the x - and y -axis and achieve spectral accuracy, we make use of Fourier transform in the xy -plane

$$\begin{pmatrix} \Omega_{s,\text{det.}}^{(\pm)} \\ \Omega_{s,\text{noise}}^{(\pm)} \end{pmatrix}_{\mathbf{k}_x \mathbf{k}_y \mathbf{z} \tau} = \sum_{\mathbf{x}, \mathbf{y}} \mathcal{F}_{\mathbf{k}_x \mathbf{k}_y}^{\mathbf{x} \mathbf{y}} \begin{pmatrix} \Omega_{s,\text{det.}}^{(\pm)} \\ \Omega_{s,\text{noise}}^{(\pm)} \end{pmatrix}_{xyz\tau},$$

here, $\mathcal{F}_{\mathbf{k}_x \mathbf{k}_y}^{\mathbf{x} \mathbf{y}}$ denote the components of the Fourier transfrom, and \mathbf{k}_x and \mathbf{k}_y indicate the Fourier components of the fields. To denote the inverse Fourier transform, we swap the

indices $(\mathcal{F}^{-1})_{\mathbf{k}_x \mathbf{k}_y}^{\mathbf{x}\mathbf{y}} = \mathcal{F}_{\mathbf{x}\mathbf{y}}^{\mathbf{k}_x \mathbf{k}_y}$. Assuming the introduced notation, the integrating scheme takes the following form:

$$\begin{pmatrix} \Omega_{s, \text{det.}}^{(+)} \\ \Omega_{s, \text{noise}}^{(+)} \end{pmatrix}_{\mathbf{x}\mathbf{y}(\mathbf{z}+1)\tau} = \mathcal{G}_{\mathbf{x}\mathbf{y}\mathbf{z}\tau}^{(+)} \sum_{\mathbf{k}_x, \mathbf{k}_y} \mathcal{F}_{\mathbf{x}\mathbf{y}}^{\mathbf{k}_x \mathbf{k}_y} \mathcal{K}_{\mathbf{k}_x \mathbf{k}_y} \begin{pmatrix} \Omega_{s, \text{det.}}^{(+)} \\ \Omega_{s, \text{noise}}^{(+)} \end{pmatrix}_{\mathbf{k}_x \mathbf{k}_y \mathbf{z}\tau} \\ + i \begin{pmatrix} \gamma n_{\mathbf{x}\mathbf{y}\mathbf{z}} \Delta V \sum_{e, g} T_{ges} \rho_{eg, \mathbf{x}\mathbf{y}\mathbf{z}\tau} \\ \sqrt{\frac{\gamma g_{s, \mathbf{x}\mathbf{y}\mathbf{z}\tau}}{2\Delta\tau}} \xi_{s, \mathbf{x}\mathbf{y}\mathbf{z}\tau}^{(+)} + \sqrt{\frac{\gamma g_{s, \mathbf{x}\mathbf{y}(\mathbf{z}+1)\tau}}{2\Delta\tau}} \xi_{s, \mathbf{x}\mathbf{y}(\mathbf{z}+1)\tau}^{(+)} \end{pmatrix}, \quad (\text{B15})$$

$$\begin{pmatrix} \Omega_{s, \text{det.}}^{(-)} \\ \Omega_{s, \text{noise}}^{(-)} \end{pmatrix}_{\mathbf{x}\mathbf{y}(\mathbf{z}+1)\tau} = \mathcal{G}_{\mathbf{x}\mathbf{y}\mathbf{z}\tau}^{(-)} \sum_{\mathbf{k}_x, \mathbf{k}_y} \mathcal{F}_{\mathbf{x}\mathbf{y}}^{\mathbf{k}_x \mathbf{k}_y} \mathcal{K}_{\mathbf{k}_x \mathbf{k}_y}^* \begin{pmatrix} \Omega_{s, \text{det.}}^{(-)} \\ \Omega_{s, \text{noise}}^{(-)} \end{pmatrix}_{\mathbf{k}_x \mathbf{k}_y \mathbf{z}\tau} \\ - i \begin{pmatrix} \gamma n_{\mathbf{x}\mathbf{y}\mathbf{z}} \Delta V \sum_{e, g} T_{egs} \rho_{ge, \mathbf{x}\mathbf{y}\mathbf{z}\tau} \\ \sqrt{\frac{\gamma g_{s, \mathbf{x}\mathbf{y}\mathbf{z}\tau}}{2\Delta\tau}} \xi_{s, \mathbf{x}\mathbf{y}\mathbf{z}\tau}^{(-)} + \sqrt{\frac{\gamma g_{s, \mathbf{x}\mathbf{y}(\mathbf{z}+1)\tau}}{2\Delta\tau}} \xi_{s, \mathbf{x}\mathbf{y}(\mathbf{z}+1)\tau}^{(-)} \end{pmatrix}. \quad (\text{B16})$$

Here, we have introduced coefficient γ from equations (B14), elementary volume $\Delta V = \Delta x \Delta y \Delta z$, atomic density on a grid $n_{\mathbf{x}\mathbf{y}\mathbf{z}}$, and two additional matrices describing absorption and diffraction upon propagation along the medium

$$\mathcal{G}_{\mathbf{x}\mathbf{y}\mathbf{z}\tau}^{(\pm)} = \exp \left[\left(\frac{\mu_{\mathbf{x}\mathbf{y}\mathbf{z}\tau}}{2} \mp i \delta_{\mathbf{x}\mathbf{y}\mathbf{z}\tau} k_0 \right) \Delta z \right]^6, \quad \mathcal{K}_{\mathbf{k}_x \mathbf{k}_y} = \exp \left[-i \frac{k_x^2 + k_y^2}{2k_0} \Delta z \right], \quad (\text{B17})$$

where $\mu_{\mathbf{x}\mathbf{y}\mathbf{z}\tau}$ and $\delta_{\mathbf{x}\mathbf{y}\mathbf{z}\tau}$ are $\mu(\mathbf{r}, t)$ and $\delta(\mathbf{r}, t)$ on a grid.

To remove run-away trajectories, we have to adopt the strategy from sec. II H to the discrete equations (B15), (B16). At each time step, we find \mathbf{xyz} -points satisfying condition (44) and transform equations (B15), (B16) in accordance with equation (45).

With the proposed scheme, we can achieve high stability and first-order accuracy for the integration of the deterministic part along the z -axis. In addition, equations (B15), (B16) can be used for integrating pump fields or recalculating the deterministic fields in equations (B6) - (B9).

5. Qualitative analysis of the noise terms

The proportionality of the noise-term increments to $\sqrt{\Delta t}$ in equations for atomic variables (B10) - (B13) is inherent for stochastic differential equations.

⁶ In general, $\mathcal{G}_{\mathbf{x}\mathbf{y}\mathbf{z}\tau}^{(+)} \neq \mathcal{G}_{\mathbf{x}\mathbf{y}\mathbf{z}\tau}^{(-)*}$, since $\mu(\mathbf{r}, t)$ and $\delta(\mathbf{r}, t)$ may depend on non-hermitian stochastic density matrices.

In contrast to the deterministic source, the noise source in equations (B15) - (B16) is not proportional to grid size Δz . Consequently, the ratio between the noise and deterministic contribution is inversely proportional to Δz . This inverse proportionality can be understood following the arguments presented for superradiance of distributed systems [26]: the smaller the grid size is, the larger the quantum fluctuations of atomic coherence are due to the finite number of the emitters within the grid voxel. In our case, the higher spatial resolution we would like to achieve, the larger the noise-term values reflecting the larger relative role of quantum effects would be, and the larger amount of realizations we would need to run in order to achieve smooth profiles for observables of interest.

Appendix C: Dipole moment. Pump and decay terms

1. Dipole moment calculations

Following [84], the dipole matrix element for transition from state $|n'l's'j'm'\rangle$ to $|nlsjm\rangle$, where $l(l')$ and $s(s')$ denote the orbital angular momentum and spin, $j(j')$ and $m(m')$ the total angular momentum and its projection, and $n(n')$ any additional quantum numbers, can be calculated as $\langle nlsjm|\hat{D}_q|n'l's'j'm'\rangle = (-1)^{j-m}\sqrt{2j+1}\begin{pmatrix} j & 1 & j' \\ -m & q & m' \end{pmatrix} \langle nlsj||D||n'l's'j'\rangle$, where \hat{D}_q is a component of the electric dipole operator, and $\langle nlsj||D||n'l's'j'\rangle$ is the reduced dipole matrix element, which in notation from Eq. (18) corresponds to $d_0/\sqrt{3}$ due to normalization.

2. Pump terms

The contribution of incoherent pumping via photoionization to eq. (50) is encompassed by the term $p_i^{(\text{pump})}$ that is given as

$$p_i^{(\text{pump})} = \sum_{\mathcal{F}'} J_{\mathcal{F}'} S_{\mathcal{F}'i}^{(\text{ground})} \rho^{(\text{ground})}, \quad (\text{C1})$$

where $S_{\mathcal{F}'i}^{(\text{ground})}$ contains photoionization cross sections and is defined in terms of their numerical values in Appendix D, and $J_{\mathcal{F}}$ denotes the flux of field mode, namely, pump (\mathcal{P}) or emitted SF field with any of the polarization: $\mathcal{F} = \{\mathcal{P}, \Omega_{-1}, \Omega_{+1}\}$. For the emitted field

modes, the flux is defined as

$$J_{\Omega_\sigma} = \frac{dN_{\Omega_\sigma}}{d\tau dS} = \frac{2\varepsilon_0 c_0 \mathcal{E}_\sigma^{(+)} \mathcal{E}_\sigma^{(-)}}{\hbar\omega_0} = \frac{\Omega_\sigma^{(+)} \Omega_\sigma^{(-)}}{\frac{3}{8\pi} \lambda^2 \Gamma_r}, \quad (C2)$$

where $N_{\mathcal{F}}$ is the number of photons in field mode \mathcal{F} , $\lambda = 0.154 \text{ nm}$ is the wavelength of emitted radiation, and $\Gamma_r = 0.60 \text{ eV}$ is the $1s^{-1} - 2p^{-1}$ radiative decay width. The pump electric field \mathcal{P} can be defined as

$$\mathcal{P}(\mathbf{r}, t) = \mathcal{P}^{(+)}(\mathbf{r}, t) e^{i(k_P z - \omega_P t)} \hat{\mathbf{e}}_y + \mathcal{P}^{(-)}(\mathbf{r}, t) e^{-i(k_P z - \omega_P t)} \hat{\mathbf{e}}_y^*, \quad (C3)$$

where $\omega_P = k_P c_0$ is the pump carrier frequency, and it was taken into account that the pump field is linearly polarized along the y axis with $\hat{\mathbf{e}}_y$ denoting the unit polarization vector. Since the FEL field is modeled as temporally coherent and only interacts with the atomic system via incoherent processes, the positive- and negative-frequency components of its slowly-varying amplitude $\mathcal{P}^{(\pm)}$ are connected through $\mathcal{P}^{(+)} = \mathcal{P}^{(-)*}$. Thus the pump field flux can be defined as

$$J_{\mathcal{P}} = \frac{dN_{\mathcal{P}}}{d\tau dS} = \frac{2\varepsilon_0 c_0 |\mathcal{P}|^2}{\hbar\omega_P}, \quad (C4)$$

where we denote $\mathcal{P}^{(+)} = \mathcal{P}$.

3. Isotropic fluorescence decay terms

The dimensionless coefficients describing the relative spontaneous isotropic fluorescence decay widths are encompassed in $G_{ij}^{(\text{rad.})}$. They can be obtained using the definition

$$\gamma_{r,ij} = \frac{\omega_0^3}{3\pi\hbar\varepsilon_0 c_0^3} \sum_{q=-1}^1 \left| \langle i | \hat{D}_q | j \rangle \right|^2. \quad (C5)$$

Using Wigner-Eckart theorem in a similar way as it was applied to arrive to (48), (49), for the present case we obtain

$$G_{ge}^{(\text{rad.})} = \begin{pmatrix} 0 & 0 & 0 & 0 & \frac{1}{3} & 0 \\ 0 & 0 & 0 & 0 & \frac{2}{9} & \frac{1}{9} \\ 0 & 0 & 0 & 0 & \frac{1}{9} & \frac{2}{9} \\ 0 & 0 & 0 & 0 & 0 & \frac{1}{3} \\ 0 & 0 & 0 & 0 & 0 & 0 \\ 0 & 0 & 0 & 0 & 0 & 0 \end{pmatrix}, \quad (C6)$$

here the nomenclature for the sequence of levels according to (12), (47) was used.

4. Decay and decoherence terms

The matrix M_{ij} that describes decay and decoherence processes in (50) has contribution due atomic decay channels and due to ionisation caused by external fields:

$$M_{ij} = M_{ij}^{(\text{decay})} + M_{ij}^{(\text{ion})}. \quad (\text{C7})$$

The first term includes the natural decay widths of the $1s^{-1}$ (K) and $2p_{3/2}^{-1}$ (L_3) levels, and can be expressed as

$$M_{ij}^{(\text{decay})} = \Gamma_{L_3} e_i^{(L_3)} \otimes e_j^{(L_3)} + \Gamma_K e_i^{(K)} \otimes e_j^{(K)} + \frac{\Gamma_{L_3} + \Gamma_K}{2} \left(e_i^{(L_3)} \otimes e_j^{(K)} + e_i^{(K)} \otimes e_j^{(L_3)} \right), \quad (\text{C8})$$

where \otimes denotes the outer product of vectors. Auxiliary vectors to denote the K and L_3 levels are defined as

$$e_i^{(L_3)} = (1, 1, 1, 1, 0, 0)^T, \quad e_i^{(K)} = (0, 0, 0, 0, 1, 1)^T, \quad (\text{C9})$$

with T denoting the transpose.

The decay of states (12) due to photoionization with both the pump and emitted field can be represented as:

$$M_{ij}^{(\text{ion})} = -\frac{\gamma_i^{(\text{ion.})} + \gamma_j^{(\text{ion.})}}{2}, \quad \gamma_i^{(\text{ion.})} = \sum_{\mathcal{F}'} S_{\mathcal{F}'i}^{(\text{ion.})} J_{\mathcal{F}'}, \quad (\text{C10})$$

where the cross-section matrix $S_{\mathcal{F}'i}^{(\text{ion.})}$ is defined in Appendix D.

5. Evolution of auxiliary states

The pump term (C1) depends on the population of the ground state $\rho^{(\text{ground})}$. It evolves according to

$$\frac{\partial}{\partial \tau} \rho^{(\text{ground})} = - \sum_{i', \mathcal{F}'} S_{\mathcal{F}'i'}^{(\text{ground})} J_{\mathcal{F}'} \rho^{(\text{ground})}. \quad (\text{C11})$$

The absorption of the pump is influenced also by the cumulative population of singly-ionized states. To this aim, an auxiliary level (other) is introduced that evolves as

$$\frac{\partial}{\partial \tau} \rho^{(\text{other})} = - \sum_{\mathcal{F}'} \rho^{(\text{other})} S_{\mathcal{F}'}^{(\text{other})} J_{\mathcal{F}'} + \sum_{\mathcal{F}'} \rho^{(\text{ground})} S_{\mathcal{F}'-1}^{(\text{ground})} J_{\mathcal{F}'}, \quad (\text{C12})$$

with $S_{\mathcal{F}'-1}^{(\text{ground})}$ denoting the last column of the cross-section matrix. Both levels interact with the system of $1s^{-1}$ and $2p_{3/2}^{-1}$ states only via nonresonant photoionization described by $S_{\mathcal{F}'i'}^{(\text{ground})}$ and $S_{\mathcal{F}'}^{(\text{other})}$ (see Appendix D for numerical values).

6. Pump propagation

Besides decreasing in intensity, the absorption upon propagation of the pump radiation results in the changing of its temporal [72] and spatial profile. This change has significant effect on the evolution of the x-ray superfluorescence, hence modeling of the pump-pulse propagation is essential for our aims. Propagation equations for the emitted field modes can be obtained from Eqs. (34) – (35) by modifying the r.h.s. Namely, since the pump field is only coupled to the atomic and ionic states via nonresonant photoabsorption, it is sufficient to describe response of the atoms in terms of absorption coefficient:

$$\left[\frac{\partial}{\partial z} - \frac{i}{2k_{\mathcal{P}}} \left(\frac{\partial^2}{\partial x^2} + \frac{\partial^2}{\partial y^2} \right) \right] \mathcal{P} = -\frac{\kappa_{\mathcal{P}}}{2} \mathcal{P}. \quad (\text{C13})$$

The absorption coefficients for the different field modes can be represented as:

$$\kappa_{\mathcal{F}} = n \sum_{i'} \left(\rho^{(\text{ground})} S_{\mathcal{F}i'}^{(\text{ground})} + \rho^{(\text{other})} S_{\mathcal{F}}^{(\text{other})} + \rho_{i'i'} S_{\mathcal{F}i'}^{(\text{ion.})} + \sigma_{\mathcal{F}}^{(\text{compound})} \right), \quad (\text{C14})$$

where n is the number density of copper atoms, and $\sigma_{\mathcal{F}}^{(\text{compound})}$ is the cross section for photoionization of elements composing the liquid compound other than copper (see Appendix D for details).

Appendix D: Photoionization cross sections

Photoionization cross sections included in the model of Cu-K $_{\alpha_1}$ superfluorescence are also calculated with the GRASP [85] and RATIP [86] atomic codes, however in this case additional calculations are required to obtain the partial cross section corresponding to individual magnetic sublevels included in the model. In accordance with the 6-level model composing the core Cu-K $_{\alpha_1}$ system (47), the valence $4s$ electron is omitted. The ground state configuration of the copper atom in this approximation is [Ar] $3d^{10} 1S_0$, and the ionic states of interest are [Ar] $3d^{10} 1s^{-1} 2S_{1/2}$ and [Ar] $3d^{10} 2p^{-1} 2P_{3/2}$.

Photoionization of the ground atomic state, which is related to the pumping of population inversion, is described in terms of partial ionization cross section encompassed in the matrix

$$S_{\mathcal{F}i}^{(\text{ground})} = \begin{pmatrix} 0.27 \sigma_{\mathcal{P},2p}^{(g)} & 0.23 \sigma_{\mathcal{P},2p}^{(g)} & 0.23 \sigma_{\mathcal{P},2p}^{(g)} & 0.27 \sigma_{\mathcal{P},2p}^{(g)} & 0.5 \sigma_{\mathcal{P},1s}^{(g)} & 0.5 \sigma_{\mathcal{P},1s}^{(g)} & \sigma_{\mathcal{P},o}^{(g)} \\ 0.12 \sigma_{\Omega,2p}^{(g)} & 0.18 \sigma_{\Omega,2p}^{(g)} & 0.28 \sigma_{\Omega,2p}^{(g)} & 0.42 \sigma_{\Omega,2p}^{(g)} & 0 & 0 & \sigma_{\Omega,o}^{(g)} \\ 0.42 \sigma_{\Omega,2p}^{(g)} & 0.28 \sigma_{\Omega_{+1},2p}^{(g)} & 0.18 \sigma_{\Omega,2p}^{(g)} & 0.12 \sigma_{\Omega,2p}^{(g)} & 0 & 0 & \sigma_{\Omega,o}^{(g)} \end{pmatrix}. \quad (\text{D1})$$

Here $\sigma_{\mathcal{F},i}^{(g)}$ represents the cross section for photoionization with field mode $\mathcal{F} = \{\mathcal{P}, \Omega_{-1}, \Omega_{+1}\}$ where an electron is ionized from the $1s$ subshell if $i = 1s$, or from $2p_{3/2}$ subshell if $i = 2p$. If $i = o$, the ground state is ionized to one of the states encompassed in the auxilliary level (other). The sequence of levels is as in (47) but with added level (other) at the end of the sequence, i.e.

$$2p_{\frac{3}{2},m=-\frac{3}{2}}, 2p_{\frac{3}{2},m=-\frac{1}{2}}, 2p_{\frac{3}{2},m=\frac{1}{2}}, 2p_{\frac{3}{2},m=\frac{3}{2}}, 1s_{\frac{1}{2},m=-\frac{1}{2}}, 1s_{\frac{1}{2},m=\frac{1}{2}}, (\text{other}).$$

Cross sections for photoionization of ionic levels composing the core $\text{K}\alpha$ system are described by

$$S_{\mathcal{F}i}^{(\text{ion.})} = \begin{pmatrix} 1.05 \sigma_{\mathcal{P},2p}^{(i)} & 0.95 \sigma_{\mathcal{P},2p}^{(i)} & 0.95 \sigma_{\mathcal{P},2p}^{(i)} & 1.05 \sigma_{\mathcal{P},2p}^{(i)} & \sigma_{\mathcal{P},1s}^{(i)} & \sigma_{\mathcal{P},1s}^{(i)} \\ 0.70 \sigma_{\Omega,2p}^{(i)} & 0.83 \sigma_{\Omega,2p}^{(i)} & 1.06 \sigma_{\Omega,2p}^{(i)} & 1.41 \sigma_{\Omega,2p}^{(i)} & 0.75 \sigma_{\Omega,1s}^{(i)} & 1.25 \sigma_{\Omega,1s}^{(i)} \\ 1.41 \sigma_{\Omega,2p}^{(i)} & 1.06 \sigma_{\Omega,2p}^{(i)} & 0.83 \sigma_{\Omega,2p}^{(i)} & 0.70 \sigma_{\Omega,2p}^{(i)} & 1.25 \sigma_{\Omega,1s}^{(i)} & 0.75 \sigma_{\Omega,1s}^{(i)} \end{pmatrix}. \quad (\text{D2})$$

Here $\sigma_{\mathcal{F},i}^{(i)}$ denotes the total photoionization cross section of level i with field mode \mathcal{F} , where $i = 1s$ denotes level $1s^{-1}$, and $i = 2p$ denotes level $2p_{3/2}^{-1}$. The sequence of levels is assumed to be the same as described above.

Photoionization of the additional level (other), which describes the population of states of Cu^+ other than $1s_{\frac{1}{2},m}$ and $2p_{\frac{3}{2},m}$, is included via

$$S_{\mathcal{F}}^{(\text{other})} = \left(\sigma_{\mathcal{P}}^{(o)} \sigma_{\Omega}^{(o)} \sigma_{\Omega}^{(o)} \right)^T, \quad (\text{D3})$$

where $\sigma_{\mathcal{F}}^{(o)}$ is the effective total cross section for ionization of this additional level with field mode \mathcal{F} , and T denotes the transpose of the vector.

Since the target medium is a solution of copper nitrate, photoionization of atoms other than copper also causes significant absorption of both the pump and emitted field, and has to be included in the model. Since cross sections for ionization of additional elements composing the solution are smaller than those for copper, we assume that only a small

fraction of these atoms is ionized and their population is equal to 1 throughout the target at all times. The effective photoionization cross section due to the compound elements other than copper can be expressed as

$$\sigma_{\mathcal{F}}^{(\text{compound})} = \sum_{\text{el.}} N_{\text{el.}} \sigma_{\mathcal{F},\text{el.}}, \quad (\text{D4})$$

where $\sum_{\text{el.}}$ runs over these additional elements, $N_{\text{el.}}$ is the number of atoms of a given element per one copper atom, and $\sigma_{\mathcal{F},\text{el.}}$ is the corresponding cross section for ionization with field mode \mathcal{F} . Elements present in the compound are hydrogen, oxygen (el. = O) and nitrogen (el. = N), however, since the photon energy of the pump and emitted fields is 8 – 9 keV, which is almost three orders of magnitude above the ionization threshold of hydrogen, the corresponding cross sections are negligible.

Numerical values of photoionization cross sections for all the processes included in the simulation of Cu-K $_{\alpha_1}$ system are presented in Table I. For the 8-molar solution of copper nitrate, the number of atoms in the compound per one copper atom is $N_{\text{O}} = 13$ and $N_{\text{N}} = 2$. The details of calculations are given below.

| Parameter | Value [nm 2] | Parameter | Value [nm 2] |
|--|-----------------------|--|-----------------------|
| $\sigma_{\mathcal{P},1s}^{(\text{g})}$ | 2.53×10^{-6} | $\sigma_{\mathcal{P},1s}^{(\text{i})}$ | 4.75×10^{-7} |
| $\sigma_{\mathcal{P},2p}^{(\text{g})}$ | 1.04×10^{-7} | $\sigma_{\mathcal{P},2p}^{(\text{i})}$ | 3.02×10^{-7} |
| $\sigma_{\mathcal{P},o}^{(\text{g})}$ | 3.23×10^{-7} | $\sigma_{\Omega,1s}^{(\text{i})}$ | 6.53×10^{-7} |
| $\sigma_{\Omega,2p}^{(\text{g})}$ | 1.52×10^{-7} | $\sigma_{\Omega,2p}^{(\text{i})}$ | 4.15×10^{-7} |
| $\sigma_{\Omega,o}^{(\text{g})}$ | 4.34×10^{-7} | $\sigma_{\mathcal{P}}^{(\text{o})}$ | 3.27×10^{-7} |
| | | $\sigma_{\text{Omega}}^{(\text{o})}$ | 4.58×10^{-7} |
| $\sigma_{\mathcal{P},\text{O}}$ | 2.00×10^{-8} | $\sigma_{\mathcal{P},\text{N}}$ | 1.11×10^{-8} |
| $\sigma_{\Omega,\text{O}}$ | 2.75×10^{-8} | $\sigma_{\Omega,\text{N}}$ | 1.55×10^{-8} |

TABLE I: Values of photoionization cross sections included in the model of the Cu-K $_{\alpha_1}$ system.

1. Calculation of partial photoionization cross sections for magnetic sublevels

The wave function of the outgoing electron can be expanded in terms of partial waves as [87]

$$\begin{aligned} |\psi_c\rangle &= \sum_{l=0}^{\infty} \sum_{m_l=-l}^l |lm_lsm_s\rangle Y_{lm_l}^*(\vartheta_k, \varphi_k) \\ &= \sum_{l=0}^{\infty} \sum_{m_l=-l}^l \sum_{j_f=|l-s|}^{l+s} \sum_{m_f=-j_f}^{j_f} \langle j_f m_f | lm_lsm_s \rangle |(ls)j_f m_f\rangle Y_{lm_l}^*(\vartheta_k, \varphi_k), \end{aligned} \quad (\text{D5})$$

where $s = 1/2$ is the electron spin and m_s its projection, l orbital angular momentum and m_l its projection, and ϑ_k and φ_k are the polar and azimuthal angles associated with the wave vector of the electron. The final state product function combining the ion and electron can then be expanded in terms of the total angular momentum of the system as [84]

$$\begin{aligned} |\psi_c\rangle |J_f M_f\rangle &= \sum_{l, m_l} \sum_{j_f, m_f} \langle j_f m_f | lm_lsm_s \rangle \sum_{J=|j_f - J_f|}^{j_f + J_f} \sum_{M=-J}^J \langle JM | j_f m_f J_f M_f \rangle \\ &\quad \times |[(ls)j_f J_f] JM\rangle Y_{lm_l}^*(\vartheta_k, \varphi_k), \end{aligned} \quad (\text{D6})$$

where J_f is the total angular momentum of the ion and M_f its projection, j_f and m_f are the total angular momentum of the electron and its projection, and J and M correspond to the combined system of the ion and electron. The photoionization cross section is proportional to the absolute square of photoionization amplitudes $\langle J_f M_f | \langle \psi_c | \hat{D}_q | J_i M_i \rangle$, where J_i is the total angular momentum of the initial state, M_i its projection, and \hat{D}_q is a component of the electric dipole operator.

In the case of photoionization from the ground state to a selected state of Cu^+ with given J_f and M_f by field with polarization mode q , $J_i = M_i = 0$ and the cross sections of interest are

$$\begin{aligned} \sigma(J_f, M_f, q) &= \xi \sum_{m_s} \int d\Omega_k |\langle J_f M_f | \langle \psi_c | \hat{D}_q | 00 \rangle|^2 \\ &= \xi \sum_l \sum_{j_f} \langle 1q | j_f (q - M_f) J_f M_f \rangle^2 | \langle [(ls)j_f J_f] 1 | D | 0 \rangle |^2, \end{aligned} \quad (\text{D7})$$

where $d\Omega_k = \sin \vartheta_k d\vartheta_k d\varphi_k$, and ξ is a constant factor that depends on the specific form of the dipole transition operator and unit system used in the calculation (conventions differ between different references and atomic codes). This expression determines the individual

cross sections in the last two rows of $S_{\mathcal{F}i}^{(\text{ground})}$ corresponding to ionization with the circularly polarized modes of the emitted field. In the derivation of Eq. (D7) the following properties of spherical harmonics and Clebsch-Gordan coefficients were used [84]:

$$\int d\Omega_k Y_{lm_l}(\vartheta_k, \varphi_k) Y_{l'm'_l}^*(\vartheta_k, \varphi_k) = \delta_{l,l'} \delta_{m_l, m'_l}, \quad (\text{D8a})$$

$$\sum_{m_1, m_2} \langle JM | j_1 m_1 j_2 m_2 \rangle \langle j_1 m_1 j_2 m_2 | J' M' \rangle = \delta_{J,J'} \delta_{M,M'}, \quad (\text{D8b})$$

$$\langle j_1 m_1 j_2 m_2 | JM \rangle \neq 0 \Leftrightarrow m_1 + m_2 = M. \quad (\text{D8c})$$

In the chosen coordinate system, the pump pulse is linearly polarized along the y axis. Cross sections for ionization with the pump field can be expressed as

$$\begin{aligned} \sigma(J_f, M_f, y) &= \xi \sum_{m_s} \int d\Omega_k |\langle J_f M_f | \langle \psi_c | \frac{1}{\sqrt{2}} (\hat{D}_{-1} + \hat{D}_{+1}) | 00 \rangle|^2 \\ &= \frac{1}{2} [\sigma(J_f, M_f, q = -1) + \sigma(J_f, M_f, q = +1)], \end{aligned} \quad (\text{D9})$$

and correspond to the individual cross sections in the first row of $S_{\mathcal{F}i}^{(\text{ground})}$.

Reduced dipole matrix elements $\langle [(ls)j_f J_f] 1 | |D| |0 \rangle$ (also called photoionization amplitudes) are part of the output of the RATIP code [86], and can be used to calculate the prefactors in matrix $S_{\mathcal{F}i}^{(\text{ground})}$. The code also outputs cross sections, which are calculated for unpolarized light and are averaged over initial states and summed over final states. Unpolarized light can be treated as a linear combination of two incoherent linearly polarized beams of equal intensity [88]. The calculated cross sections, which correspond to the total cross sections $\sigma_{\mathcal{F},i}^{(\text{g})}$, can in our notation be written as

$$\sigma(J_f) = \frac{1}{2} \sum_{q=-1,1} \sum_{M_f} \sigma(J_f, M_f, q) = \xi \sum_l \sum_{j_f} |\langle [(ls)j_f J_f] 1 | |D| |0 \rangle|^2. \quad (\text{D10})$$

In the case of Cu^+ to Cu^{++} ionization, the cross sections of interest are

$$\begin{aligned} \sigma(J_i, M_i, q) &= \zeta \sum_{J_f} \sum_{M_f} \sum_{m_s} \int d\Omega_k |\langle J_f M_f | \langle \psi_c | \hat{D}_q | J_i M_i \rangle|^2 \\ &= \zeta \sum_{J_f} \sum_l \sum_{j_f} \sum_J \langle J(M_i + q) | J_i M_i 1q \rangle^2 |\langle [(ls)j_f J_f] J | |D| |J_i \rangle|^2, \end{aligned} \quad (\text{D11})$$

where J_i is the total angular momentum of the initial ionic state of Cu^+ and M_i its projection. These cross sections correspond to the individual cross sections in the last two rows of $S_{\mathcal{F}i}^{(\text{ion.})}$. The cross section for ionization with the pump pulse can similarly as above be expressed as

$$\sigma(J_i, M_i, y) = \frac{1}{2} [\sigma(J_i, M_i, q = -1) + \sigma(J_i, M_i, q = +1)], \quad (\text{D12})$$

and corresponds to the individual cross sections in the first row of $S_{\mathcal{F}_i}^{(\text{ion.})}$. Again, the photoionization cross sections and amplitudes are calculated with the RATIP code. In our notation these cross sections can be expressed as

$$\begin{aligned}\sigma(J_i) &= \frac{1}{2} \sum_{q=-1,1} \frac{1}{2J_i + 1} \sum_{M_i} \sigma(J_i, M_i, q) \\ &= \zeta \frac{1}{3(2J_i + 1)} \sum_{J_f} \sum_l \sum_{j_f} \sum_J (2J + 1) |\langle [(ls)j_f J_f] J | D | J_i \rangle|^2,\end{aligned}\quad (\text{D13})$$

in the derivation of which the following symmetry relation was used [84]:

$$\langle j_1 m_1 j_2 m_2 | JM \rangle = (-1)^{j_2 + m_2} \sqrt{\frac{2J + 1}{2j_1 + 1}} \langle j_2 (-m_2) JM | j_1 m_1 \rangle. \quad (\text{D14})$$

These cross sections also correspond to the total cross sections $\sigma_{\mathcal{F},i}^{(\text{i})}$. Because of the averaging over the initial states, the relation between the partial and total cross sections is $\sum_{M_i} \sigma(J_i, M_i, q) = (2J_i + 1)\sigma(J_i)$.

- [1] Jens Als-Nielsen and Des McMorrow, [Elements of Modern X-ray Physics](#), 1st ed. (Wiley, 2011).
- [2] Paul Emma [et al.](#), “First lasing and operation of an angstrom-wavelength free-electron laser,” [Nat. Photon.](#) **4**, 641–647 (2009).
- [3] Tetsuya Ishikawa [et al.](#), “A compact x-ray free-electron laser emitting in the sub-angstrom region,” [Nat. Photon.](#) **6**, 540–544 (2012).
- [4] Heung-Sik Kang [et al.](#), “Hard x-ray free-electron laser with femtosecond-scale timing jitter,” [Nat. Photon.](#) **11**, 708–713 (2017).
- [5] Christopher Milne [et al.](#), “SwissFEL: The Swiss X-ray Free Electron Laser,” [Applied Sciences](#) **7**, 720 (2017).
- [6] Hans Weise and Winfried Decking, “Commissioning and First Lasing of the European XFEL,” [Proceedings of the 38th Int. Free Electron Laser Conf. FEL2017](#), 5 pages (2018).
- [7] Christoph Bostedt, Sébastien Boutet, David M. Fritz, Zhirong Huang, Hae Ja Lee, Henrik T. Lemke, Aymeric Robert, William F. Schlotter, Joshua J. Turner, and Garth J. Williams, “Linac Coherent Light Source: The first five years,” [Reviews of Modern Physics](#) **88**, 015007 (2016).

[8] Uwe Bergmann, Vittal Yachandra, and Junko Yano, [X-Ray Free Electron Lasers](#), Energy and Environment Series (The Royal Society of Chemistry, 2017) pp. P001–463.

[9] Jonathan P. Marangos, “Accessing the quantum spatial and temporal scales with XFELs,” [Nature Reviews Physics](#) **2**, 332–334 (2020).

[10] Uwe Bergmann, Jan Kern, Robert W. Schoenlein, Philippe Wernet, Vittal K. Yachandra, and Junko Yano, “Using X-ray free-electron lasers for spectroscopy of molecular catalysts and metalloenzymes,” [Nature Reviews Physics](#) **3**, 264–282 (2021).

[11] Eberhard J Jaeschke, Shaukat Khan, Jochen R Schneider, and Jerome B Hastings, [Synchrotron light sources and free-electron lasers](#) (Springer Cham, 2016).

[12] Linda Young, Kiyoshi Ueda, Markus Gühr, Philip H Bucksbaum, Marc Simon, Shaul Mukamel, Nina Rohringer, Kevin C Prince, Claudio Masciovecchio, Michael Meyer, Artem Rudenko, Daniel Rolles, Christoph Bostedt, Matthias Fuchs, David A Reis, Robin Santra, Henry Kapteyn, Margaret Murnane, Heide Ibrahim, François Légaré, Marc Vrakking, Marcus Isinger, David Kroon, Mathieu Gisselbrecht, Anne L’Huillier, Hans Jakob Wörner, and Stephen R Leone, “Roadmap of ultrafast x-ray atomic and molecular physics,” [Journal of Physics B: Atomic, Molecular and Optical Physics](#) **51**, 032003 (2018).

[13] Nina Rohringer, Duncan Ryan, Richard A. London, Michael Purvis, Felicie Albert, James Dunn, John D. Bozek, Christoph Bostedt, Alexander Graf, Randal Hill, Stefan P. Hau-Riege, and Jorge J. Rocca, “Atomic inner-shell x-ray laser at 1.46 nanometres pumped by an x-ray free-electron laser,” [Nature](#) **481**, 488–491 (2012).

[14] Clemens Weninger, Michael Purvis, Duncan Ryan, Richard A. London, John D. Bozek, Christoph Bostedt, Alexander Graf, Gregory Brown, Jorge J. Rocca, and Nina Rohringer, “Stimulated electronic x-ray raman scattering,” [Phys. Rev. Lett.](#) **111**, 233902 (2013).

[15] Hitoki Yoneda, Yuichi Inubushi, Kazunori Nagamine, Yurina Michine, Haruhiko Ohashi, Hiroyokatsu Yumoto, Kazuto Yamauchi, Hidekazu Mimura, Hikaru Kitamura, Tetsuo Katayama, Tetsuya Ishikawa, and Makina Yabashi, “Atomic inner-shell laser at 1.5-ångström wavelength pumped by an x-ray free-electron laser,” [Nature](#) **524**, 446–449 (2015).

[16] Yu Zhang, Thomas Kroll, Clemens Weninger, Yurina Michine, Franklin D. Fuller, Diling Zhu, Roberto Alonso-Mori, Dimosthenis Sokaras, Alberto A. Lutman, Aliaksei Halavanau, Claudio Pellegrini, Andrei Benediktovitch, Makina Yabashi, Ichiro Inoue, Yuichi Inubushi, Taito Osaka, Jumpei Yamada, Ganguli Babu, Devashish Salpekar, Farheen N. Sayed, Pulickel M.

Ajayan, Jan Kern, Junko Yano, Vittal K. Yachandra, Hitoki Yoneda, Nina Rohringer, and Uwe Bergmann, “Generation of intense phase-stable femtosecond hard X-ray pulse pairs,” *Proceedings of the National Academy of Sciences* **119**, e2119616119 (2022).

[17] Thomas Kroll, Clemens Weninger, Roberto Alonso-Mori, Dimosthenis Sokaras, Diling Zhu, Laurent Mercadier, Vinay P. Majety, Agostino Marinelli, Alberto Lutman, Marc W. Guetg, Franz-Josef Decker, Sébastien Boutet, Andy Aquila, Jason Koglin, Jake Koralek, Daniel P. DePonte, Jan Kern, Franklin D. Fuller, Ernest Pastor, Thomas Fransson, Yu Zhang, Junko Yano, Vittal K. Yachandra, Nina Rohringer, and Uwe Bergmann, “Stimulated x-ray emission spectroscopy in transition metal complexes,” *Phys. Rev. Lett.* **120**, 133203 (2018).

[18] Thomas Kroll, Clemens Weninger, Franklin D. Fuller, Marc W. Guetg, Andrei Benediktovitch, Yu Zhang, Agostino Marinelli, Roberto Alonso-Mori, Andy Aquila, Mengning Liang, Jason E. Koglin, Jake Koralek, Dimosthenis Sokaras, Diling Zhu, Jan Kern, Junko Yano, Vittal K. Yachandra, Nina Rohringer, Alberto Lutman, and Uwe Bergmann, “Observation of Seeded Mn K β Stimulated X-Ray Emission Using Two-Color X-Ray Free-Electron Laser Pulses,” *Physical Review Letters* **125**, 037404 (2020).

[19] Markus Kowalewski, Benjamin P. Fingerhut, Konstantin E. Dorfman, Kochise Bennett, and Shaul Mukamel, “Simulating Coherent Multidimensional Spectroscopy of Nonadiabatic Molecular Processes: From the Infrared to the X-ray Regime,” *Chemical Reviews* **117**, 12165–12226 (2017).

[20] Aliaksei Halavanau, Andrei Benediktovitch, Alberto A. Lutman, Daniel DePonte, Daniele Cocco, Nina Rohringer, Uwe Bergmann, and Claudio Pellegrini, “Population inversion X-ray laser oscillator,” *Proceedings of the National Academy of Sciences* **117**, 15511–15516 (2020).

[21] Zhirong Huang and Ronald D. Ruth, “Fully coherent x-ray pulses from a regenerative-amplifier free-electron laser,” *Phys. Rev. Lett.* **96**, 144801 (2006).

[22] Gabriel Marcus, Alex Halavanau, Zhirong Huang, Jacek Krzywinski, James MacArthur, Rachel Margraf, Tor Raubenheimer, and Diling Zhu, “Refractive Guide Switching a Regenerative Amplifier Free-Electron Laser for High Peak and Average Power Hard X Rays,” *Physical Review Letters* **125**, 254801 (2020).

[23] Kwang-Je Kim, Yuri Shvyd’ko, and Sven Reiche, “A proposal for an x-ray free-electron laser oscillator with an energy-recovery linac,” *Phys. Rev. Lett.* **100**, 244802 (2008).

[24] R. R. Lindberg, K.-J. Kim, Yu. Shvyd’ko, and W. M. Fawley, “Performance of the x-ray free-

electron laser oscillator with crystal cavity," [Physical Review Special Topics - Accelerators and Beams](#) **14**, 010701 (2011).

[25] R. H. Dicke, "Coherence in spontaneous radiation processes," [Phys. Rev.](#) **93**, 99–110 (1954).

[26] M. Gross and S. Haroche, "Superradiance: An essay on the theory of collective spontaneous emission," [Physics Reports](#) **93**, 301 – 396 (1982).

[27] M. G. Benedict, A. M. Ermolaev, V. A. Malyshev, I. V. Sokolov, and E. D. Trifonov, [Super-radiance: Multiatom Coherent Emission](#), 1st ed., edited by M.G Benedict (CRC Press, 2018).

[28] Michael Gegg and Marten Richter, "Efficient and exact numerical approach for many multi-level systems in open system CQED," [New Journal of Physics](#) **18**, 043037 (2016).

[29] Nathan Shammah, Shahnawaz Ahmed, Neill Lambert, Simone De Liberato, and Franco Nori, "Open quantum systems with local and collective incoherent processes: Efficient numerical simulations using permutational invariance," [Physical Review A](#) **98**, 063815 (2018).

[30] V. Sukharnikov, S. Chuchurka, A. Benediktovitch, and N. Rohringer, "Second quantization of open quantum systems in Liouville space," [ArXiv e-prints](#) (2022), arXiv:2207.14234 [physics.quant-ph].

[31] F. Robicheaux, "Theoretical study of early-time superradiance for atom clouds and arrays," [Physical Review A](#) **104**, 063706 (2021).

[32] Eric Sierra, Stuart J. Masson, and Ana Asenjo-Garcia, "Dicke Superradiance in Ordered Lattices: Dimensionality Matters," [Physical Review Research](#) **4**, 023207 (2022).

[33] Robert W. Boyd, [Nonlinear optics](#), 4th ed. (Academic Press, San Diego, 2020).

[34] Sudhakar Prasad and Roy J. Glauber, "Initiation of superfluorescence in a large sphere," [Physical Review A](#) **31**, 1583–1597 (1985).

[35] G. Hazak, "Amplification of spontaneous emission and coherence in three-dimensional systems," [Physical Review A](#) **42**, 4169–4176 (1990).

[36] Jamal T. Manassah, "Cooperative radiation from atoms in different geometries: decay rate and frequency shift," [Advances in Optics and Photonics](#) **4**, 108 (2012).

[37] Q. H. F. Vrehen and M. F. H. Schuurmans, "Direct measurement of the effective initial tipping angle in superfluorescence," [Phys. Rev. Lett.](#) **42**, 224–227 (1979).

[38] E. A. Watson, H. M. Gibbs, F. P. Mattar, M. Cormier, Y. Claude, S. L. McCall, and M. S. Feld, "Quantum fluctuations and transverse effects in superfluorescence," [Physical Review A](#)

27, 1427–1434 (1983).

[39] J. Andreasen and Hui Cao, “Finite-Difference Time-Domain Formulation of Stochastic Noise in Macroscopic Atomic Systems,” *Journal of Lightwave Technology* **27**, 4530–4535 (2009).

[40] Andreas Pusch, Sebastian Wuestner, Joachim M. Hamm, Kosmas L. Tsakmakidis, and Ortwin Hess, “Coherent Amplification and Noise in Gain-Enhanced Nanoplasmonic Metamaterials: A Maxwell-Bloch Langevin Approach,” *ACS Nano* **6**, 2420–2431 (2012).

[41] G.M. Slavcheva, J.M. Arnold, and R.W. Ziolkowski, “FDTD Simulation of the Nonlinear Gain Dynamics in Active Optical Waveguides and Semiconductor Microcavities,” *IEEE Journal of Selected Topics in Quantum Electronics* **10**, 1052–1062 (2004).

[42] O. Larroche, D. Ros, A. Klisnick, A. Sureau, C. Möller, and H. Guennou, “Maxwell-bloch modeling of x-ray-laser-signal buildup in single- and double-pass configurations,” *Phys. Rev. A* **62**, 043815 (2000).

[43] Hsing-Ta Chen, Tao E. Li, Maxim Sukharev, Abraham Nitzan, and Joseph E. Subotnik, “Ehrenfest+R dynamics. I. A mixed quantum–classical electrodynamics simulation of spontaneous emission,” *The Journal of Chemical Physics* **150**, 044102 (2019).

[44] Tao E. Li, Hsing-Ta Chen, and Joseph E. Subotnik, “Comparison of Different Classical, Semiclassical, and Quantum Treatments of Light–Matter Interactions: Understanding Energy Conservation,” *Journal of Chemical Theory and Computation* **15**, 1957–1973 (2019).

[45] Tao E. Li, Abraham Nitzan, Maxim Sukharev, Todd Martinez, Hsing-Ta Chen, and Joseph E. Subotnik, “Mixed quantum-classical electrodynamics: Understanding spontaneous decay and zero-point energy,” *Physical Review A* **97**, 032105 (2018).

[46] Clemens Weninger and Nina Rohringer, “Transient-gain photoionization x-ray laser,” *Phys. Rev. A* **90**, 063828 (2014).

[47] Chunhai Lyu, Stefano M. Cavaletto, Christoph H. Keitel, and Zoltán Harman, “Narrow-band hard-x-ray lasing with highly charged ions,” *Scientific Reports* **10**, 9439 (2020).

[48] E. Oliva, M. Fajardo, L. Li, M. Pittman, T. T. T. Le, J. Gautier, G. Lambert, P. Velarde, D. Ros, S. Sebban, and Ph Zeitoun, “A proposal for multi-tens of gw fully coherent femtosecond soft x-ray lasers,” *Nature Photonics* **6**, 764–767 (2012).

[49] A. Depresseux, E. Oliva, J. Gautier, F. Tissandier, G. Lambert, B. Vodungbo, J-P. Goddet, A. Tafzi, J. Nejdl, M. Kozlova, G. Maynard, H. T. Kim, K. Ta Phuoc, A. Rousse, P. Zeitoun, and S. Sebban, “Demonstration of a circularly polarized plasma-based soft-x-ray laser,” *Phys.*

Rev. Lett. **115**, 083901 (2015).

- [50] Yu-Hung Kuan and Wen-Te Liao, “Transition between amplified spontaneous emission and superfluorescence in a longitudinally pumped medium by an x-ray free-electron-laser pulse,” *Physical Review A* **101**, 023836 (2020).
- [51] S. Krušič, K. Bučar, A. Mihelič, and M. Žitnik, “Collective effects in the radiative decay of the 2^1p state in helium,” *Phys. Rev. A* **98**, 013416 (2018).
- [52] Andrei Benediktovitch, Vinay P. Majety, and Nina Rohringer, “Quantum theory of superfluorescence based on two-point correlation functions,” *Physical Review A* **99**, 013839 (2019).
- [53] L. Mercadier, A. Benediktovitch, C. Weninger, M. A. Blessenohl, S. Bernitt, H. Bekker, S. Dobrodey, A. Sanchez-Gonzalez, B. Erk, C. Bomme, R. Boll, Z. Yin, V. P. Majety, R. Steinbrügge, M. A. Khalal, F. Penent, J. Palaudoux, P. Lablanquie, A. Rudenko, D. Rolles, J. R. Crespo López-Urrutia, and N. Rohringer, “Evidence of Extreme Ultraviolet Superfluorescence in Xenon,” *Physical Review Letters* **123**, 023201 (2019).
- [54] Š. Krušič, A. Mihelič, K. Bučar, and M. Žitnik, “Self-induced splitting of x-ray emission lines,” *Physical Review A* **102**, 013102 (2020).
- [55] Stasis Chuchurka, “Quantum stochastic trajectories for particles and fields based on positive p representation,” to be submitted () .
- [56] Stasis Chuchurka, “Stochastic methodology for superfluorescence i: General theory,” to be submitted () .
- [57] Stasis Chuchurka, “Stochastic methodology for superfluorescence ii: Mean field theory,” to be submitted () .
- [58] P. Varga and P. Török, “The gaussian wave solution of Maxwell’s equations and the validity of scalar wave approximation,” *Optics Communications* **152**, 108–118 (1998).
- [59] Saša Bajt, Mauro Prasciolu, Holger Fleckenstein, Martin Domaracký, Henry N Chapman, Andrew J Morgan, Oleksandr Yefanov, Marc Messerschmidt, Yang Du, Kevin T Murray, Valerio Mariani, Manuela Kuhn, Steven Aplin, Kanupriya Pande, Pablo Villanueva-Perez, Karolina Stachnik, Joe PJ Chen, Andrzej Andrejczuk, Alke Meents, Anja Burkhardt, David Pennicard, Xiaojing Huang, Hanfei Yan, Evgeny Nazaretski, Yong S Chu, and Christian E Hamm, “X-ray focusing with efficient high-NA multilayer Laue lenses,” *Light: Science & Applications* **7**, 17162–17162 (2018).
- [60] S. Matsuyama, T. Inoue, J. Yamada, J. Kim, H. Yumoto, Y. Inubushi, T. Osaka, I. Inoue,

T. Koyama, K. Tono, H. Ohashi, M. Yabashi, T. Ishikawa, and K. Yamauchi, “Nanofocusing of x-ray free-electron laser using wavefront-corrected multilayer focusing mirrors,” *Scientific Reports* **8**, 17440 (2018).

[61] L. D. Landau and E. M. Lifshitz, *Quantum mechanics: non-relativistic theory* (Elsevier, 1977).

[62] P Deuar and P D Drummond, “First-principles quantum dynamics in interacting Bose gases II: stochastic gauges,” *Journal of Physics A: Mathematical and General* **39**, 2723–2755 (2006).

[63] Piotr Deuar, “First-principles quantum simulations of many-mode open interacting Bose gases using stochastic gauge methods,” *arXiv:cond-mat/0507023* (2005), arXiv: cond-mat/0507023.

[64] Kenan Li, Michael Wojcik, and Chris Jacobsen, “Multislice does it all—calculating the performance of nanofocusing X-ray optics,” *Optics Express* **25**, 1831 (2017).

[65] David G. Voelz and Michael C. Roggeman, “Digital simulation of scalar optical diffraction: revisiting chirp function sampling criteria and consequences,” *Applied Optics* **48**, 6132 (2009).

[66] Zoltan Jurek, Sang-Kil Son, Beata Ziaja, and Robin Santra, “*XMDYN* and *XATOM*: versatile simulation tools for quantitative modeling of X-ray free-electron laser induced dynamics of matter,” *Journal of Applied Crystallography* **49**, 1048–1056 (2016).

[67] Andrei Benediktovitch, Laurent Mercadier, Olivier Peyrusse, Andreas Przystawik, Tim Laermann, Bruno Langbehn, Cédric Bomme, Benjamin Erk, Jonathan Correa, Caroline Mossé, Daniel Rolles, Sven Toleikis, Maximilian Bucher, Christoph F. O. Bostedt, Alvaro Sanchez-Gonzalez, Stepan Dobrodey, Michael A. Blesenohl, Alexander Nelde, Maria Müller, Daniela Rupp, Thomas Möller, José R. Crespo López-Urrutia, and Nina Rohringer, “Amplified spontaneous emission in the extreme ultraviolet by expanding xenon clusters,” *Physical Review A* **101**, 063412 (2020).

[68] E.L. Saldin, E.A. Schneidmiller, and M.V. Yurkov, “Coherence properties of the radiation from X-ray free electron laser,” *Optics Communications* **281**, 1179–1188 (2008).

[69] Bob Nagler et al., “Turning solid aluminium transparent by intense soft X-ray photoionization,” *Nature Physics* **5**, 693–696 (2009).

[70] Hitoki Yoneda, Yuichi Inubushi, Makina Yabashi, Tetsuo Katayama, Tetsuya Ishikawa, Haruhiko Ohashi, Hirokatsu Yumoto, Kazuto Yamauchi, Hidekazu Mimura, and Hikaru Kitamura, “Saturable absorption of intense hard X-rays in iron,” *Nature Communications* **5**, 5080 (2014).

[71] D.S. Rackstraw, O. Cricosta, S.M. Vinko, B. Barbrel, T. Burian, J. Chalupský, B.I. Cho,

H.-K. Chung, G.L. Dakovski, K. Engelhorn, V. Hájková, P. Heimann, M. Holmes, L. Juha, J. Krzywinski, R.W. Lee, S. Toleikis, J.J. Turner, U. Zastrau, and J.S. Wark, “Saturable Absorption of an X-Ray Free-Electron-Laser Heated Solid-Density Aluminum Plasma,” [Physical Review Letters](#) **114**, 015003 (2015).

[72] Ichiro Inoue, Yuichi Inubushi, Taito Osaka, Jumpei Yamada, Kenji Tamasaku, Hitoki Yoneda, and Makina Yabashi, “Shortening X-Ray Pulse Duration via Saturable Absorption,” [Physical Review Letters](#) **127**, 163903 (2021).

[73] Sebastian Cardoch, Fabian Trost, Howard A. Scott, Henry N. Chapman, Carl Caleman, and Nicusor Timneanu, “Decreasing ultrafast x-ray pulse durations with saturable absorption and resonant transitions,” [Phys. Rev. E](#) **107**, 015205 (2023).

[74] Peter D. Drummond and Mark Stephen Hillery, [The quantum theory of nonlinear optics](#) (Cambridge University Press, 2014).

[75] Marlan O. Scully and M. Suhail Zubairy, [Quantum Optics](#) (Cambridge University Press, 1997).

[76] G I Peters and L Allen, “Amplified spontaneous emission. IV. Beam divergence and spatial coherence,” [Journal of Physics A: General Physics](#) **5**, 546–554 (1972).

[77] O Svelto, S Taccheo, and C Svelto, “Analysis of amplified spontaneous emission: some corrections to the Linford formula,” [Optics Communications](#) **149**, 277–282 (1998).

[78] V. Kocharyan, S. Cameron, K. Lehmann, R. Lucht, R. Miles, Y. Rostovtsev, W. Warren, G. R. Welch, and M. O. Scully, “Gain-swept superradiance applied to the stand-off detection of trace impurities in the atmosphere,” [Proceedings of the National Academy of Sciences](#) **102**, 7806–7811 (2005).

[79] François Salin and Jeff Squier, “Gain guiding in solid-state lasers,” [Optics Letters](#) **17**, 1352 (1992).

[80] C. Pellegrini, A. Marinelli, and S. Reiche, “The physics of x-ray free-electron lasers,” [Reviews of Modern Physics](#) **88**, 015006 (2016).

[81] Christian Brosseau, [Fundamentals of polarized light: a statistical optics approach](#) (Wiley, New York, 1998).

[82] A Crubellier, S Liberman, and P Pillet, “Superradiance theory and random polarisation,” [Journal of Physics B: Atomic and Molecular Physics](#) **19**, 2959–2971 (1986).

[83] Crispin W. Gardiner, [Handbook of Stochastic Methods](#), edited by Hermann Haken, Springer Series in Synergetics, Vol. 13 (Springer Berlin Heidelberg, Berlin, Heidelberg, 2004).

- [84] D. M. Brink and G. R. Satchler, Angular Momentum (Clarendon Press, 1994).
- [85] F.A. Parpia, C.Froese Fischer, and I.P. Grant, “Grasp92: A package for large-scale relativistic atomic structure calculations,” *Computer Physics Communications* **94**, 249 – 271 (1996).
- [86] S. Fritzsch, “Ratip – a toolbox for studying the properties of open-shell atoms and ions,” *Journal of Electron Spectroscopy and Related Phenomena* **114-116**, 1155 – 1164 (2001), proceeding of the Eight International Conference on Electronic Spectroscopy and Structure.
- [87] Charles J. Joachain, Quantum Collision Theory (North-Holland Publishing Company, 1975).
- [88] Steven T. Manson and Anthony F. Starace, “Photoelectron angular distributions: energy dependence for s subshells,” *Reviews of Modern Physics* **54**, 389–405 (1982).